nanomaterials

MDPI

Article

Facile Synthesis of Cobalt Ferrite ($CoFe_2O_4$) Nanoparticles in the Presence of Sodium Bis (2-ethyl-hexyl) Sulfosuccinate and Their Application in Dyes Removal from Single and Binary Aqueous Solutions

Claudia Maria Simonescu [1,*], Alina Tătăruş [1,2,*], Daniela Cristina Culiţă [3,*], Nicolae Stănică [3], Bogdan Butoi [4] and Andrei Kuncser [5]

1 Department of Analytical Chemistry and Environmental Engineering, Faculty of Applied Chemistry and Materials Science, Politehnica University of Bucharest, Polizu Street, No. 1-7, District 1, 011061 Bucharest, Romania
2 National Research and Development Institute for Industrial Ecology, INCD-ECOIND, Drumul Podul Dambovitei Street, No. 71-73, District 6, 060652 Bucharest, Romania
3 Ilie Murgulescu Institute of Physical Chemistry, 202 Splaiul Independentei, 060021 Bucharest, Romania; nstanica@icf.ro
4 National Institute for Laser, Plasma and Radiation Physics, 077125 Măgurele, Romania; bogdan.butoi@inflpr.ro
5 National Institute for Materials Physics, Atomistilor Street 405, 077125 Măgurele, Romania; andrei.kuncser@infim.ro
* Correspondence: claudiamaria_simonescu@yahoo.com or claudia.simonescu@upb.ro (C.M.S.); alina.tatarus@yahoo.com (A.T.); danaculita@yahoo.co.uk (D.C.C.); Tel.: +40-753-071-418 (C.M.S.); +60-764-000-710 (A.T.); +40-765-309-363 (D.C.C.)

Citation: Simonescu, C.M.; Tătăruş, A.; Culiţă, D.C.; Stănică, N.; Butoi, B.; Kuncser, A. Facile Synthesis of Cobalt Ferrite ($CoFe_2O_4$) Nanoparticles in the Presence of Sodium Bis (2-ethyl-hexyl) Sulfosuccinate and Their Application in Dyes Removal from Single and Binary Aqueous Solutions. *Nanomaterials* **2021**, *11*, 3128. https://doi.org/10.3390/nano11113128

Academic Editors: George Z. Kyzas and Sherif A. El-Safty

Received: 26 October 2021
Accepted: 16 November 2021
Published: 19 November 2021

Abstract: A research study was conducted to establish the effect of the presence of sodium bis-2-ethyl-hexyl-sulfosuccinate (DOSS) surfactant on the size, shape, and magnetic properties of cobalt ferrite nanoparticles, and also on their ability to remove anionic dyes from synthetic aqueous solutions. The effect of the molar ratio cobalt ferrite to surfactant (1:0.1; 1:0.25 and 1:0.5) on the physicochemical properties of the prepared cobalt ferrite particles was evaluated using different characterization techniques, such as FT-IR spectroscopy, X-ray diffraction (XRD), scanning electron microscopy (SEM), transmission electron microscopy (TEM), N_2 adsorption-desorption analysis, and magnetic measurements. The results revealed that the surfactant has a significant impact on the textural and magnetic properties of $CoFe_2O_4$. The capacity of the synthesized $CoFe_2O_4$ samples to remove two anionic dyes, Congo Red (CR) and Methyl Orange (MO), by adsorption from aqueous solutions and the factors affecting the adsorption process, such as contact time, concentration of dyes in the initial solution, pH of the media, and the presence of a competing agent were investigated in batch experiments. Desorption experiments were performed to demonstrate the reusability of the adsorbents.

Keywords: anionic dyes adsorption; Congo Red; Methyl Orange; magnetic adsorbents; surfactant effects

1. Introduction

With the rapid growth of industrialization and the increase of human needs, the global production of products that require coloring and the volume of wastewater containing dyes have increased. Dyes are colored natural or synthetic organic substances that absorb light in the visible range of the spectrum and have the property of giving color to other substances or materials. More than 100,000 dyes with an annual production of over 7 × 105 tones/year are commercially available [1]. Two thirds of the dyes are used in the textile industry [2] and an important volume of dye-containing wastewater is released into the environment. The negative effects of dyes are observed in natural ecosystems and on human health. Dyes

are characterized by high optical and thermal stability, which makes their persistence in the environment to be ongoing for a long time. In aquatic ecosystems, dyes consume the dissolved oxygen, absorb and reflect the light and negatively influence the photosynthesis and growth of bacteria, as well as the aquatic life and food chain in these ecosystems. Many of the dyes are toxic, mutagenic, and carcinogenic and cause allergies in the organisms. The chronic and/or acute effects of dyes on exposed living organisms depend on the dye level and on the exposure time. As a result, the removal and recovery of dyes from water is a priority, as even low concentrations can cause serious damage to living organisms and the environment. Congo Red (CR) and Methyl Orange (MO) are two synthetic anionic azo dyes highly soluble in water and ethanol that are persistent and difficult to biodegrade after their release into the environment. The low biodegradability of CR and MO is due to their complex molecular structure and the presence of the azo group (N=N). They are widely used in the textile, printing, wood, paper, leather, plastic, pharmaceutical and food processing industries for diagnosis purposes, and as pH indicators in research laboratories [3,4].

Traditional and non-conventional measures and methods are involved in dye removal from water and wastewater. As traditional methods widely applied to remove CR and MO from water, aqueous solutions and wastewater can be mentioned: coagulation and flocculation [5,6], adsorption [7,8], advanced oxidation techniques [9], electrochemical oxidation [10], photo Fenton process [11], photocatalytic degradation [12], and membrane-based processes [13,14]. Unconventional methods used to remove CR and MO for aqueous effluents are: biosorption [15,16], bioremediation [17], biodegradation [18], microwave-enforced sorption processes [19], sonocatalytic degradation [20], and ultrasound-assisted adsorption [8]. Numerous adsorbents such as: activated carbon and its composites [21,22], biochar [23,24], layered double hydroxide (LDH) [7,8], metallic oxides and their composites [25,26], calcium aluminate hydrates [27], zeolites and their composites [6], clays [28,29], magnetic materials [24,30], hydroxyapatite and its derivatives [31,32], synthetic polymeric materials [6,33], natural polymers [34,35], metal-organic frameworks [14,36], and industrial waste [37,38] have been applied for CR and MO removal. Magnetic materials are an important class of adsorbent materials used to remove both organic and inorganic pollutants from wastewater. The main advantage of these types of materials is the ease of their separation from the treated water after the process of retaining pollutants by a simple application of an external magnetic field. Consequently, numerous studies have been devoted to assessing the use of diverse types of magnetic nanoparticles, such as ferrites (MFe_2O_4, M=Co, Ni, Mn, Fe, Mg, Ca, Zn) and their functionalized derivatives for dye removal and recovery [39–46]. The interesting properties of cobalt ferrite, such as physical/chemical stability, mechanical hardness, and the possibility to be easily separated/recovered from the treated water by applying a magnetic field, have led to numerous studies on the use of this material in the retention of pollutants in wastewater [39]. The main synthetic methods of cobalt ferrite are: co-precipitation, combustion, sol-gel, solid state, hydrothermal, micro-emulsion, mechanical milling, reverse micelles, spray-drying, and ultrasonic and microwave-assisted hydrothermal processes [39]. The method and the synthesis parameters have an impact on the morphological, structural, textural, and magnetic properties of cobalt ferrite. Furthermore, the experimental conditions can be modified for improving and controlling the cobalt ferrite properties. Hydrothermal synthesis methods in the presence of surfactants are of great interest due to their low cost and simplicity, but also due to the control of the size, shape, and crystalline phases of the cobalt ferrite nanoparticles. The effect of surfactants such as cetyltrimethylammonium bromide (CTAB) [47,48], oleylamine, and a mixture of oleic acid/oleylamine [49], di iso-octyl sulphosuccinate [50], oleic acid [51], and sodium dodecyl sulfate (SDS) [52] on cobalt ferrite properties have been investigated.

The objective of the present study is to explore the adsorption potential of cobalt ferrite nanoparticles prepared by a surfactant (sodium bis-2-ethyl-hexyl sulfosuccinate (DOSS))-assisted hydrothermal synthesis method. The effect of DOSS on cobalt ferrite properties such as specific surface (S_{BET}), magnetic properties and dye adsorption capacity

was investigated. Two synthetic anionic azo dyes such as Congo Red (CR) and Methyl Orange (MO) were used as model dyes for adsorption experiments in single and binary aqueous synthetic solutions. The effect of experimental conditions, kinetic assessment, adsorption mechanism, and adsorption isotherms was also investigated.

2. Materials and Methods

2.1. Materials

The cobalt ferrite samples were prepared by the use of $Fe(NO_3)_3 \cdot 9H_2O$ 99%, $Co(NO_3)_2 \cdot 6H_2O$ and sodium bis-2-ethyl-hexyl sulfosuccinate (analytical grade, Sigma Aldrich, St. Louis, MO, USA). NH_4OH 25% and HCl 35% suprapure (analytical grade, Merck KGaA Germany, Darmstadt, Germany) were used to adjust the solution's pH. The dye solutions of desired concentrations were obtained from Congo Red (CR) 99% ($C_{32}H_{22}N_6Na_2O_6S_2$) and Methyl Orange (MO) (ACS reagent, Dye content 85%, $C_{14}H_{14}N_3NaO_3S$, Sigma Aldrich). Ethyl alcohol (95%) (Sigma Aldrich, St. Louis, MO, USA) was applied as a desorbing agent. Ammonium acetate 99% and acetonitrile 99% (Merck KGaA Germany, Darmstadt, Germany) were utilized as a mobile phase for the dye's chromatographic separation and detection.

2.2. Characterization Methods and Equipment

The analytical techniques, such as Fourier transform infra-red (FT-IR) analysis, X-ray diffraction (XRD), N_2 sorption analysis, scanning electron microscopy (SEM)/transmission electron microscopy (TEM), and magnetic measurements have been involved in cobalt ferrite sample characterization.

FT/IR spectra (4000–400 cm^{-1}) were recorded on a JASCO FT/IR-4700 spectrometer (Tokyo, Japan) by the use of KBr pellets. The structural characterization (XRD analysis) was performed with a Bruker A8 Advanced diffractometer in a Bragg-Brentano configuration, equipped with a 1D LynxEye detector and an X-ray-emitting tube with a copper anode. The recording of X-ray diffractograms was performed in the range 2θ (6 ÷ 85°), with a step of 0.02° and a cumulative acquisition time of 118 s. The incident divergent beam was collimated with a 0.6 mm slit, and the K_β radiation was removed with a nickel filter leaving only the $CuK_{\alpha 1,2}$ radiation (λ_{medium} = 0.154178 nm). The calculations regarding the average crystallite size and the identification of the crystalline phases were performed using Scherrer's formula and the ICDD (International Center of Diffraction Data) database, respectively. The specific surface areas (S_{BET}) were determined from N_2 adsorption-desorption experiments at −196 °C performed on a Micromeritics ASAP 2020 automatic adsorption system (Norcross, GA, USA). The samples were degassed at 250 °C for 5 h under vacuum before analysis. SEM images were recorded on an FEI Inspect S microscope (Hillsboro, OR, USA). The samples were investigated in a high vacuum medium (<10–3 mbar), at a working distance of 10 mm, with an acceleration voltage of 25 kV, ~60 uA current). Transmission Electron Microscopy (TEM) has been involved in the morphological and structural characterization of the $CoFe_2O_4$ samples. A JEOL 2100 instrument, equipped with a LaB6 electron gun and high resolution polar piece has been used. Magnetic properties were assessed at room temperature on Lake Shore's fully integrated Vibrating Sample Magnetometer system 7404 (VSM) (Westerville, OH, USA). Batch tests were carried out at 150 rpm (rotation per minute) on a GFL 3015 orbital shaker (Burgwedel, Germany) to evaluate the cobalt ferrite adsorption capacity. The dye solution's pH was measured at room temperature on an Agilent 3200 laboratory pH-meter (Agilent Technologies, Shanghai, China).

The dye's chromatographic separation and detection were achieved on an Agilent 1200 series HPLC (Tokyo, Japan) equipped with a Diode Array Detector (DAD) that records simultaneously UV-VIS spectra (190–900 nm). The Acclaim Surfactant Plus column (150 × 3.0 mm, 3.0 μm) (Thermo Scientific, Tokyo, Japan) was utilized for chromatographic runs. The detection of dye was performed at the optimal wavelengths: λ = 506 nm (CR) and λ = 428 nm (MO). Data acquisition, processing, and reporting was carried out by the use of Agilent ChemStation software, Santa Clara, CA, USA (version B03.02). The

development of the high-performance liquid chromatographic method with diode array detector (HPLC-DAD) and experimental conditions and results for detection of CR/MO from synthetic aqueous solution are already presented in our previous works [53,54]. The chromatogram obtained from the analysis of a mixed solution of MO and CR is shown in Figure 1. The retention time for MO was approximately 6 min, while for Congo Red it was approximately 12 min.

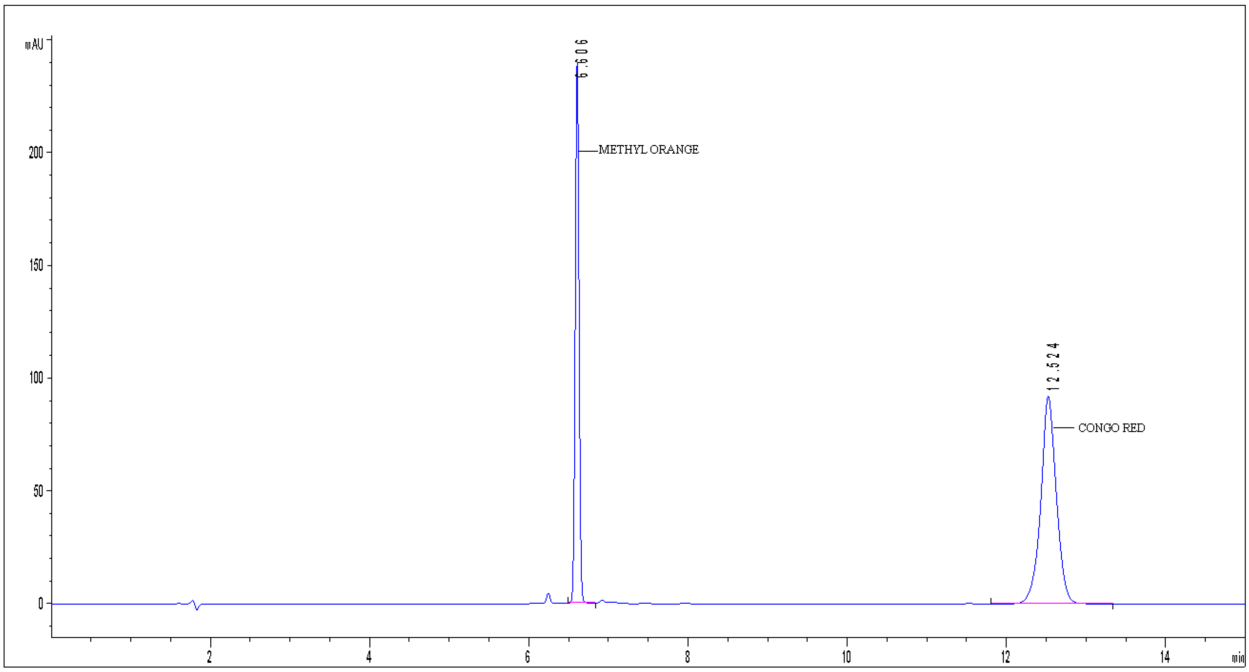

Figure 1. The chromatogram obtained from the analysis of a mixed solution of MO and CR.

2.3. Synthesis Protocol

For the synthesis of the $CoFe_2O_4$ samples, 4 experiments were performed. In the first experiment, $CoFe_2O_4$ was synthesized by coprecipitation from solution. Briefly, a solution of $Fe(NO_3)_3 \cdot 9H_2O$ (8.08 g dissolved in 100 mL distilled water) was mixed with a solution of $Co(NO_3)_2 \cdot 6H_2O$ (2.91 g dissolved in 50 mL distilled water). After stirring for 30 min at room temperature, 80 mL of 25% NH_4OH was added and the mixture was further stirred for another 2 h at 80 °C. After cooling, the precipitate was filtered and washed with distilled water and ethyl alcohol. The black powder obtained was dried for 4 h at 80 °C in an oven.

The other 3 experiments were performed using different molar ratios of cobalt ferrite to surfactant (1:0.1; 1:0.25 and 1:0.5). The surfactant was added to the reaction mixture before changing the pH (Figure 2).

Cobalt ferrite samples were denoted as follows: $CoFe_2O_4$-0—sample synthesized in the absence of surfactant, $CoFe_2O_4$-0.1, $CoFe_2O_4$-0.25, and $CoFe_2O_4$-0.5—samples synthesized in the presence of the surfactant using molar ratios of $CoFe_2O_4$:surfactant = 1:0.1, 1:0.25, and 1:0.5.

2.4. The Adsorption and Desorption Test

The effect of the experimental parameters was established in batch experiments at room temperature (22 ± 2 °C). A volume of 15 mL of azo dye (CR/MO/CR + MO) of an initial concentration of 100 $mg \cdot L^{-1}$ was contacted with 0.005 g of cobalt ferrite for 10 to 240 min at 150 rpm. After the set period of time, the adsorbent (cobalt ferrite) was separated by applying a magnetic field, and the residual concentration of the dyes in solution was determined by HPLC.

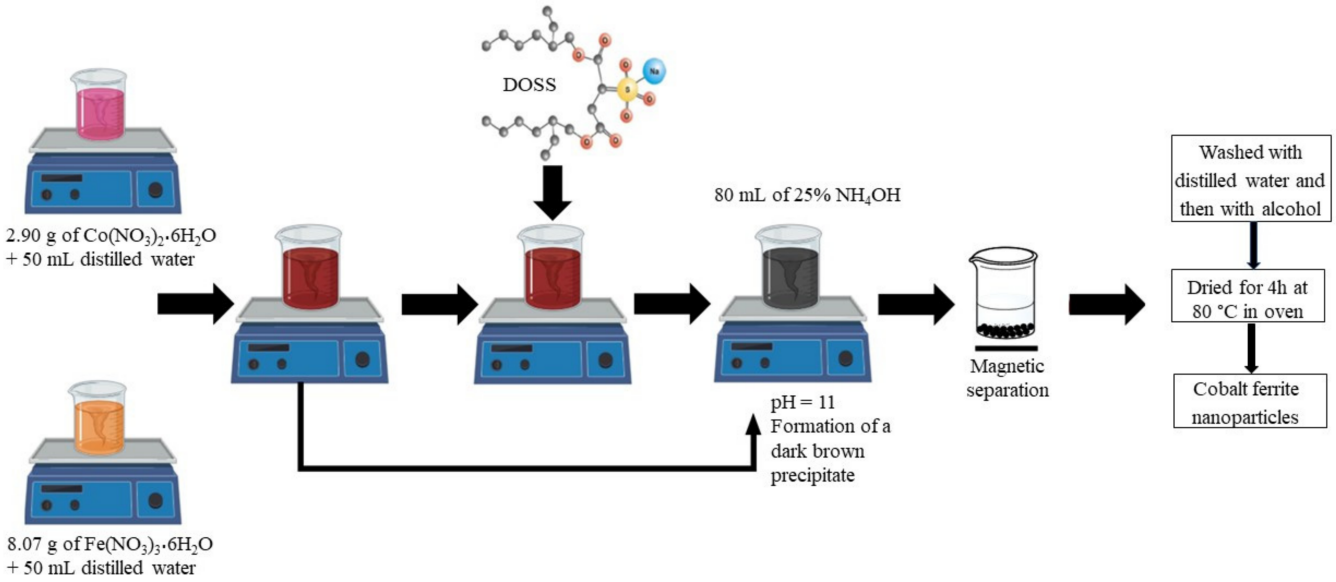

Figure 2. Synthesis of cobalt ferrite in absence and in presence of surfactant (DOSS).

The experiments regarding the effect of the dye solution's pH were performed in the range of pH between 2 and 11. An isothermal study was conducted in the dye concentration range from 5 to 100 $mg \cdot L^{-1}$. Single and binary dye solutions were analyzed. Six recyclability tests were performed by contacting 15 mL of an elution agent with 0.005 g of dye-loaded cobalt ferrite for 4 h, at room temperature and 150 rpm. The amount of CR/MO retained per gram of $CoFe_2O_4$, the desorption efficiency, and the desorption capacity are calculated with the following equations:

$$Q_t = \frac{(C_0 - C_t)V}{m} \quad (1)$$

where: Q_t is the removal capacity defined as the amount of CR/MO retained per gram of $CoFe_2O_4$ at various contact times ($mg \cdot g^{-1}$), C_0 means the CR/MO initial concentration ($mg \cdot L^{-1}$), C_t defines the CR/MO concentration after time (t) of contact with $CoFe_2O_4$ (or at various pH values) ($mg \cdot L^{-1}$), V represents the CR/MO solution volume (L), and m defines the amount of $CoFe_2O_4$ (g).

$$D(\%) = \left(\frac{Q_D}{Q_e}\right) \times 100 \quad (2)$$

where: D represents the desorption efficiency (%), Q_D means the desorption capacity estimated by Equation (3) ($mg \cdot g^{-1}$) and Qe is the adsorption capacity at equilibrium ($mg \cdot g^{-1}$).

$$Q_D = \frac{C_f}{m} \times V \quad (3)$$

where: C_f is the final concentration of CR/MO desorbed ($mg \cdot L^{-1}$), V means the eluent agent volume (L), and m constitutes the amount of $CoFe_2O_4$ loaded with CR/MO (g).

The batch tests were carried out in triplicate with a maximum experimental error of 5%.

3. Results and Discussion

3.1. Spectroscopic Characterization of $CoFe_2O_4$ Samples (FTIR Spectroscopy)

The FTIR spectra of $CoFe_2O_4$, DOSS surface-modified $CoFe_2O4$ samples, and free DOSS recorded in the range of 4000–400 cm^{-1}, are shown in Figure 3.

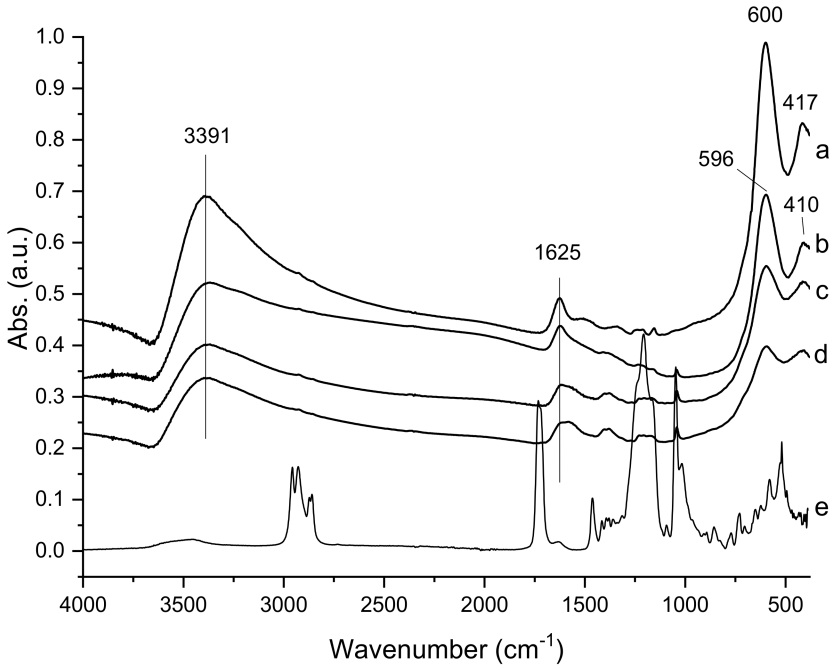

Figure 3. FTIR spectra of (a) $CoFe_2O_4$—0; (b) $CoFe_2O_4$—0.1; (c) $CoFe_2O_4$—0.25; (d) $CoFe_2O_4$—0.5; (e) DOSS.

The spectrum of $CoFe_2O_4$-0 reveals the presence of two intense absorption bands at 600 and 417 cm^{-1} which are associated with tetrahedral–A and octahedral–B sublattices of pure $CoFe_2O_4$ particles, according to the literature data [55,56]. These absorption bands confirm the presence of Co-O and Fe-O bonds in the cobalt ferrite structure. These two bands are slightly shifted to lower frequencies, 596 and 410 cm^{-1} in the spectra of the DOSS surface-modified $CoFe_2O_4$ samples. This shifting can be attributed to the changes in the length of the M-O bonds in the tetrahedral and octahedral sites [55]. The bands located at 3391 cm^{-1} and 1625 cm^{-1} are characteristic of the O–H stretching vibration and H–O–H bending vibration [55]. This indicates the presence of hydroxyl groups and water molecules absorbed on the surface of the $CoFe_2O_4$ particles. By comparing the spectra of DOSS surface-modified $CoFe_2O_4$ samples with that of free DOSS, it is clear that the other bands present in the DOSS surface-modified $CoFe_2O_4$ samples in the range of 1000–1500 cm^{-1} could be attributed to the surfactant traces entrapped in the small pores.

3.2. Structural and Morphological Characterization of $CoFe_2O_4$ Samples

X-ray diffractograms for each powder are shown in Figure 4. They are similar (therefore the same polycrystalline phases are present in all $CoFe_2O_4$ powders), the differences from one sample to another being given by the position and width of the diffraction maxima (therefore, the dimensions of the elementary cell and the average size of the crystallites differ). All diffraction maxima indicate that there is a major (98%) cubic phase of the spinelic type, $CoFe_2O_4$, according to the PDF sheet 01-080-6487, which is represented in Figure 4 by the green vertical bars. Most probably the difference of 2% could be attributed to some secondary phases such as iron or cobalt oxides.

The lattice parameter a, and the mean size (D) of the $CoFe_2O_4$ crystallites were calculated for each powder from the parameters of the maximum (311). The results are presented in Table 1. According to these values, the $CoFe_2O_4$ was synthetized as nanoparticles and the effect of the surfactant consisted of a small decrease of the particle size.

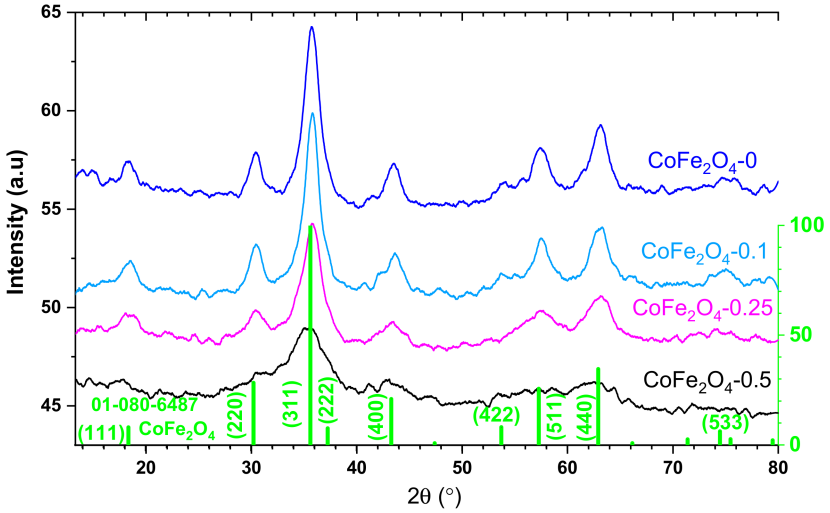

Figure 4. X-Ray diffractograms of $CoFe_2O_4$ samples.

Table 1. Textural, magnetic properties, lattice parameters and mean size of $CoFe_2O_4$ samples.

Sample	S_{BET} (m^2g^{-1})	Pore Volume (cm^3g^{-1})	Average Pore Size (nm)	M_S (emu/g)	*a* (Å)	*D* (nm)
$CoFe_2O_4$–0	186.0	0.160	3.50	33.5	8.329	5
$CoFe_2O_4$–0.1	171.3	0.170	3.66	28.5	8.329	5
$CoFe_2O_4$–0.25	175.3	0.163	3.41	20.1	8.329	4
$CoFe_2O_4$–0.5	201.7	0.216	3.35	11.7	8.392	3

Scanning electron microscopy (SEM) images of cobalt ferrite and DOSS surface-modified cobalt ferrite are shown in Figures 5–8.

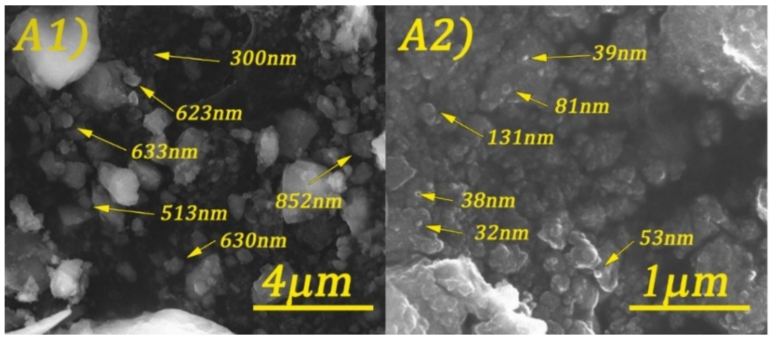

Figure 5. SEM images of $CoFe_2O_4$-0 at different magnifications: 20 kX (**A1**) and 80 kX (**A2**).

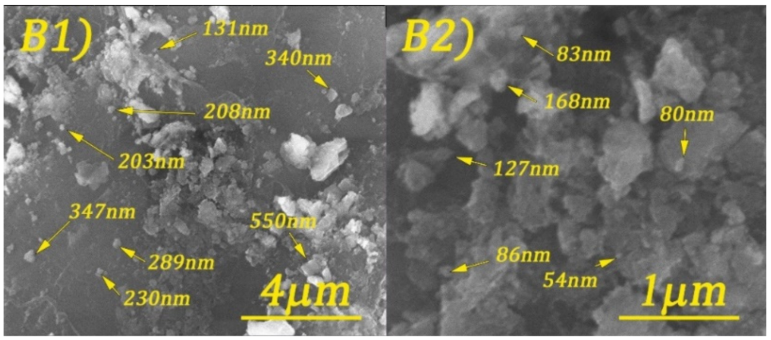

Figure 6. SEM images of $CoFe_2O_4$-0.1 at different magnifications: 20 kX (**B1**) and 80 kX (**B2**).

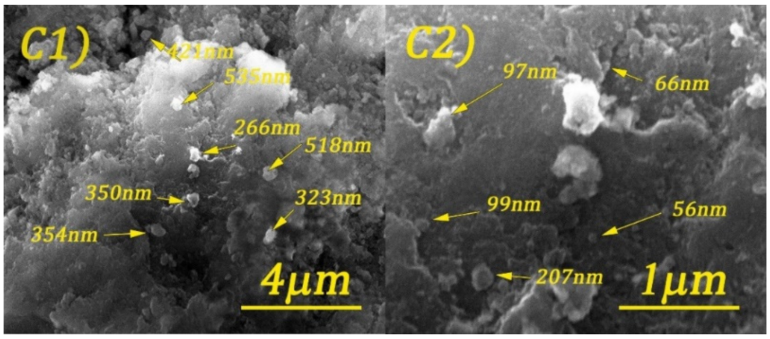

Figure 7. SEM images of $CoFe_2O_4$-0.25 at different magnifications: 20 kX (**C1**) and 80 kX (**C2**).

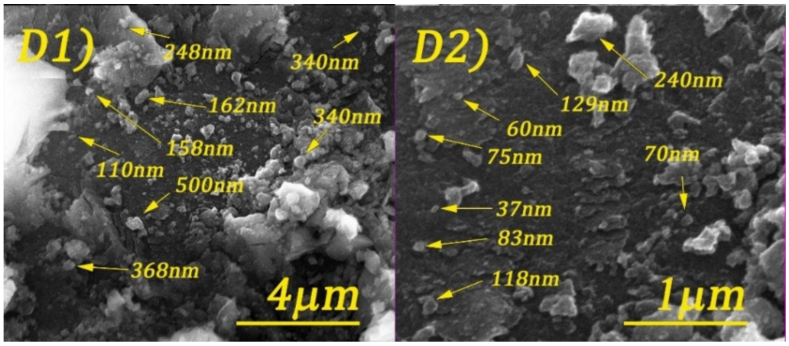

Figure 8. SEM images of $CoFe_2O_4$-0.5 at different magnifications: 20 kX (**D1**) and 80 kX (**D2**).

By analyzing the above figures, it can be seen that the $CoFe_2O_4$ was prepared in the form of conglomerates of nanometric and micrometric structures. Particle sizes range from tens of nanometers to micrometers. The effect of the surfactant is observed by the formation of much better-defined particles, but with less regular shapes.

Conventional Electron Microscopy (CTEM) images, High Resolution Transmission Electron Microscopy (HRTEM) images, and Selected Area Electron Diffraction (SAED) profiles have been obtained and are shown in Figure 9.

Statistics on nanoparticles (NPs) sizes as obtained via TEM imaging are as follows: 5.46 ± 1.54 nm for $CoFe_2O_4$-0, 5.19 ± 1.77 nm for $CoFe_2O_4$-0.1, 4.12 ± 1.03 nm for $CoFe_2O_4$-0.25, and 3.77 ± 0.64 nm for $CoFe_2O_4$-0.5. Although all samples have a similar morphology, i.e., small-faceted nanoparticles (NPs) with a general quasi-spherical aspect, with diameters roughly in the 3–6 nm range, there are some differences worth mentioning. $CoFe_2O_4$-0, $CoFe_2O_4$-0.1, and $CoFe_2O_4$-0.25 show well-crystallized, faceted nanoparticles with a mean NP size of 5–6 nm, whereas the NPs in the $CoFe_2O_4$-0.5 sample appear noticeably smaller, with a more pronounced spherical-like aspect, with an average diameter of 3–4 nm. According to SAED patterns, while all the samples present NPs crystallized in the $CoFe_2O_4$ phase, the crystallinity of the $CoFe_2O_4$-0.5 system is lower than in all other cases.

3.3. Textural Properties of $CoFe_2O_4$ Samples

The textural properties of the samples were investigated by nitrogen adsorption-desorption analysis. Figure 10 shows the N_2 sorption isotherms and the corresponding pore size distribution curves. The values of specific surface areas, total pore volumes, and average pore diameters are listed in Table 1. All isotherms are type IV according to the IUPAC classification with hysteresis loops of H2 type, which is associated with capillary condensation phenomena in mesoporous structures. The H2-type hysteresis loops indicate the presence of complex pore networks. The pore-size distribution of each sample was calculated from the desorption branch of the isotherms using the BJH model. A monomodal and narrow distribution of pore sizes for all four samples can be observed, with close average diameters ranging from 3.3 to 3.7 nm. In addition, it can be seen that

the average pore diameter slightly decreases as the amount of surfactant increases. We can assume that this behavior could be due to traces of surfactant entrapped inside the pores, as evidenced by FTIR spectra (Figure 3). Considering the intensity of the bands assigned to the surfactant in the FTIR spectra of the samples, we can say that the amount of surfactant entrapped inside the pores is directly proportional to the amount of surfactant used in the synthesis. The sample $CoFe_2O_4$–0.5 that was obtained using the largest amount of surfactant has the highest BET surface area and total pore volume, as expected, while $CoFe_2O_4$–0.1 and $CoFe_2O_4$–0.25 have lower values, but close to each other, for these two parameters. However, the surface areas and total pore volumes of all four samples are higher than those reported in other papers in which the surfactant-assisted method has been used [47].

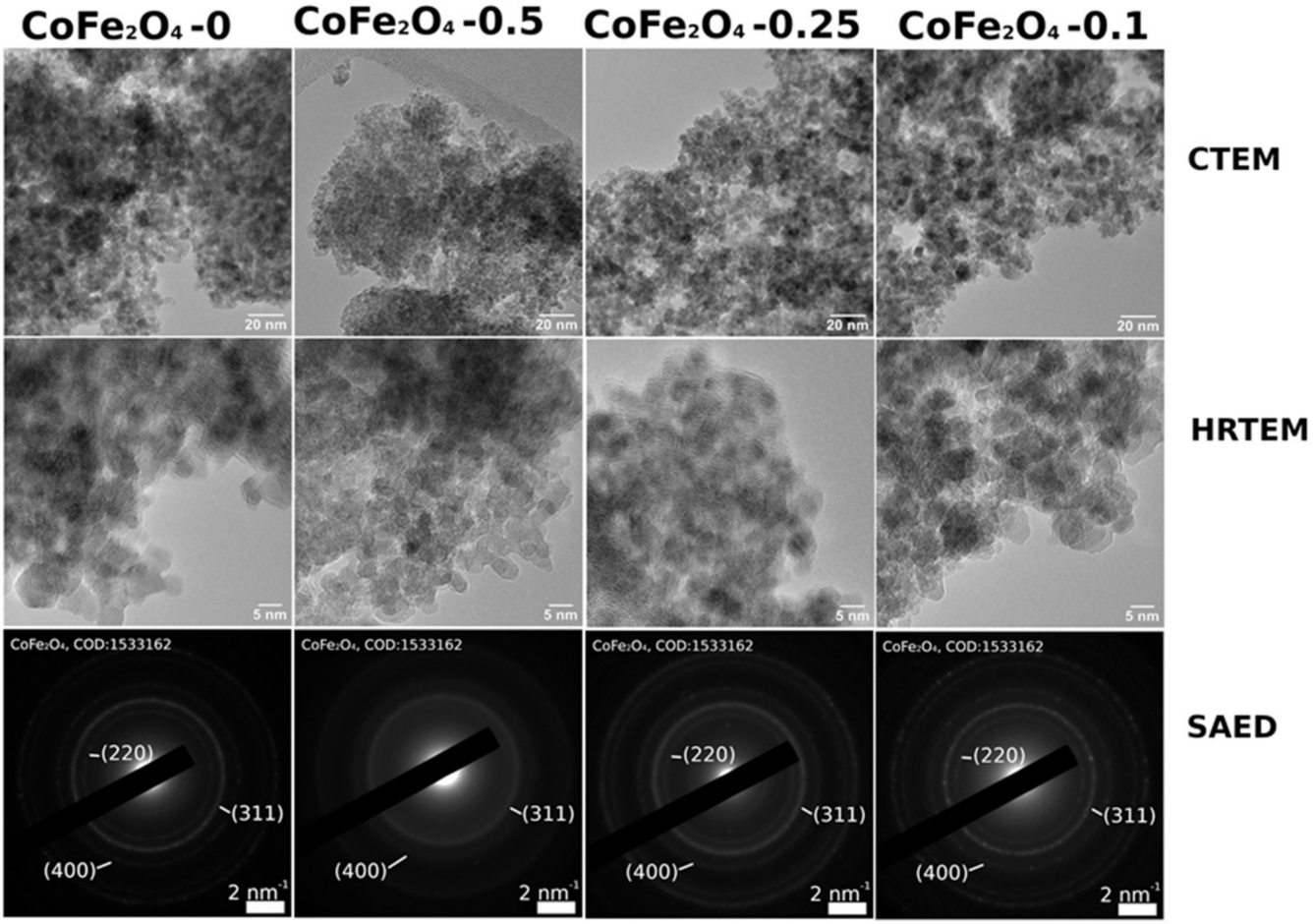

Figure 9. A comparative approach of CTEM images, HRTEM images and SAED profiles as obtained on $CoFe_2O_4$ samples.

3.4. Magnetic Characterization of $CoFe_2O_4$ Samples

Magnetic properties of the samples were measured by VSM. Figure 11 shows the magnetization versus magnetic field curves at room temperature. The zero values of remanence magnetization and coercivity observed on the hysteresis curves indicate that all $CoFe_2O_4$ samples are superparamagnetic. The calculated saturation magnetization (M_s) values (Table 1) are smaller than that reported for bulk $CoFe_2O_4$ which is 72 emu/g [57]. This can be due to the smaller size of the nanoparticles and surface effects [58]. It can be noted that the decrease of the Ms values is proportional with the amount of surfactant used in the synthesis.

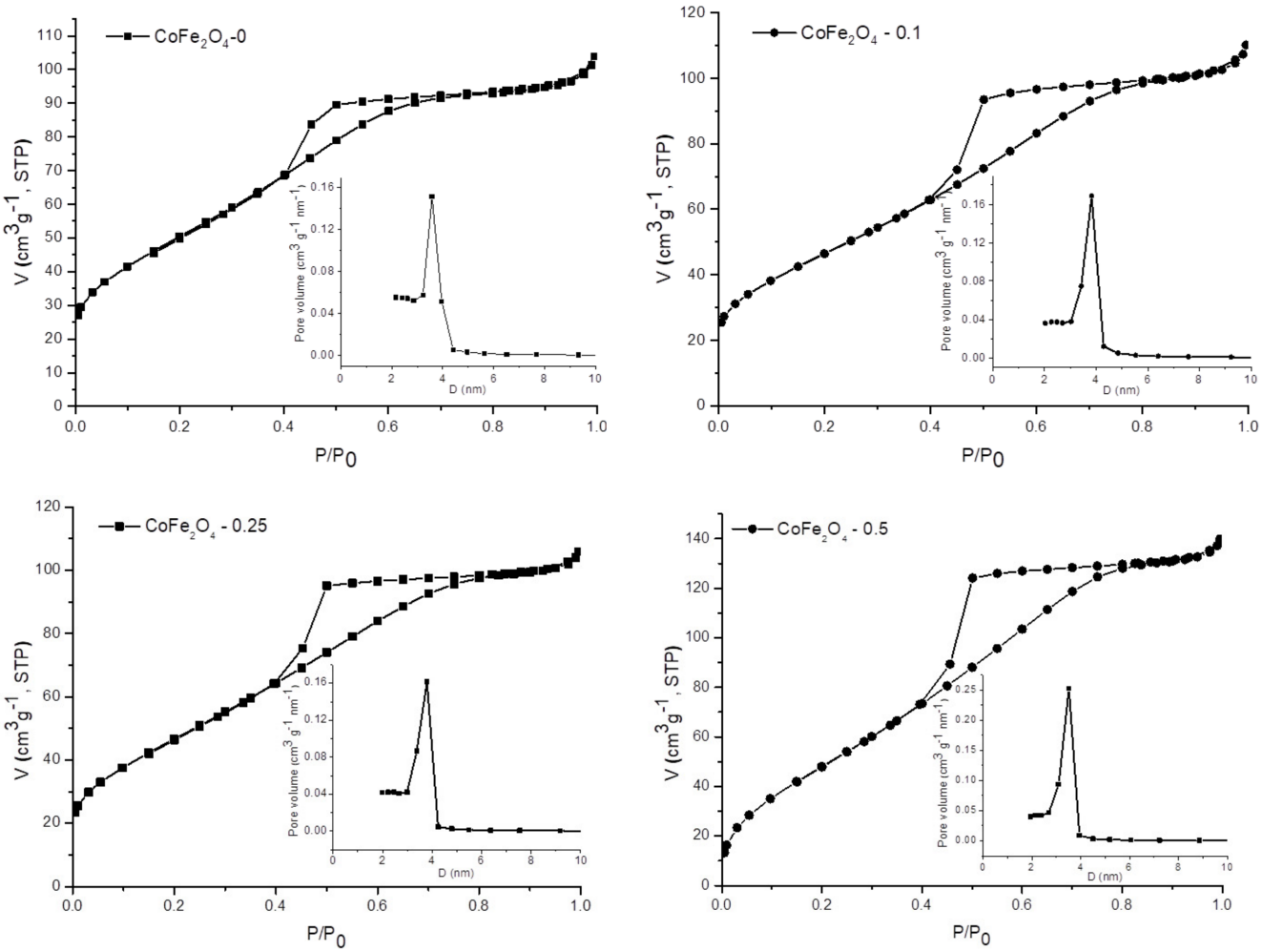

Figure 10. N_2 adsorption−desorption isotherms and pore size distribution (inset) of the samples.

3.5. Removal of Anionic Dyes from Single and Binary Solutions by Adsorption on $CoFe_2O_4$ Samples

Magnetic materials are important in the field of pollutants removal from wastewater due to their high adsorption capacity, but also to the magnetic properties which make them suitable for the separation processes. In this work, the removal of two anionic dyes, Congo Red and Methyl Orange, by adsorption on cobalt ferrite prepared in the absence/presence of surfactant was investigated in batch experiments. The effect of some important parameters on the removal capacity of these materials was studied in order to establish the influence of the amount of surfactant on their adsorption capacity and to determine the optimal conditions of the dye-removal process. Among the parameters investigated that can be mentioned are: the contact time, the solution's pH, the concentration of dyes in the initial solution, and the presence of a competing agent. To investigate the last parameter, the experiments were performed using binary solutions of Congo Red and Methyl Orange.

3.5.1. The Effect of the Contact Time and Fitting of Kinetic Models to the Adsorption Data

The effect of contact time on the adsorption capacity of the $CoFe_2O_4$ samples was studied in single and binary solutions and the results were discussed comparatively. The variation of the adsorption capacity of the $CoFe_2O_4$ samples for CR/MO from single and binary aqueous solutions as a function of the contact time is illustrated in Figure 12.

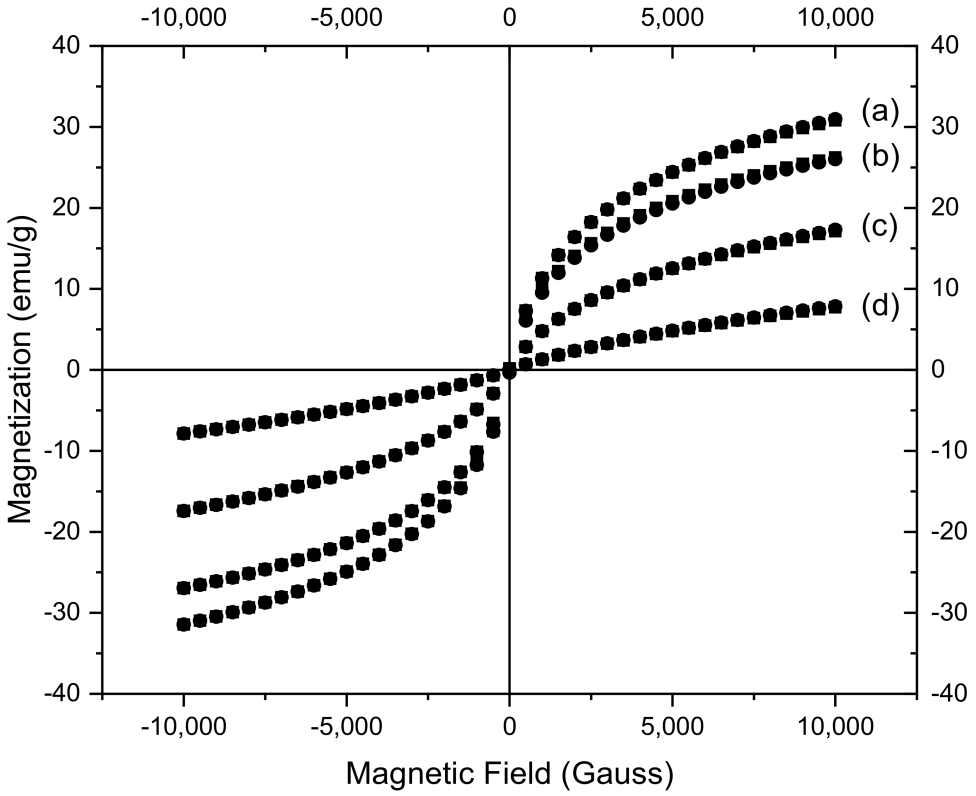

Figure 11. Magnetization curves of (a) $CoFe_2O_4$—0; (b) $CoFe_2O_4$—0.1; (c) $CoFe_2O_4$—0.25; (d) $CoFe_2O_4$—0.5 at room temperature.

Analyzing the data, it can be observed that the adsorption capacity of the cobalt ferrite samples increases with contact time. Initially, the speed of the retention process is high due to the abundance of free active centers on the surface of the cobalt ferrite. By increasing the contact time, the number of free active centers decreases, and consequently, the retention process slows down. In single solutions, a higher retention capacity for MO compared to CR for all $CoFe_2O_4$ samples synthesized in the presence of the surfactant was observed, with the highest values recorded for $CoFe_2O_4$-0.5 (MO—256.3 $mg \cdot g^{-1}$, CR—182.7 $mg \cdot g^{-1}$). It was also found that the adsorption capacity increases with the increase of the molar ratio cobalt ferrite: surfactant. In the case of MO adsorption from binary solutions (CR + MO) a decrease of the adsorption capacity compared to that obtained for single solutions was observed. It can be noted that for $CoFe_2O_4$-0 the decrease of the adsorption capacity for MO in binary solutions compared to single solutions was of 6.65 $mg \cdot g^{-1}$, while for CR the decrease was higher, 41.64 $mg \cdot g^{-1}$. For all $CoFe_2O_4$ samples synthesized in the presence of the surfactant, the decrease of the adsorption capacity was almost similar for both dyes. Based on these experiments, the contact time of 4 h was selected for further investigation.

A kinetic study was performed to determine the type of interaction between the active centers of the adsorbent and the dyes. Experimental data were evaluated by three kinetic models that are most often used to determine the mechanism involved in the adsorption process: the pseudo-first-order kinetic that is indicative for the domination of physisorption, the pseudo-second-order kinetic model that is based on the assumption that the adsorption process takes place through chemical reactions between the active centers of the adsorbent and adsorbate, and the intraparticle diffusion model which presumes that the interaction between the pollutant and active sites of the adsorbent is instantaneous relative to diffusion steps and consequently, these diffusion steps control the overall rate [59]. The equations of the three kinetic models are shown in Table 2.

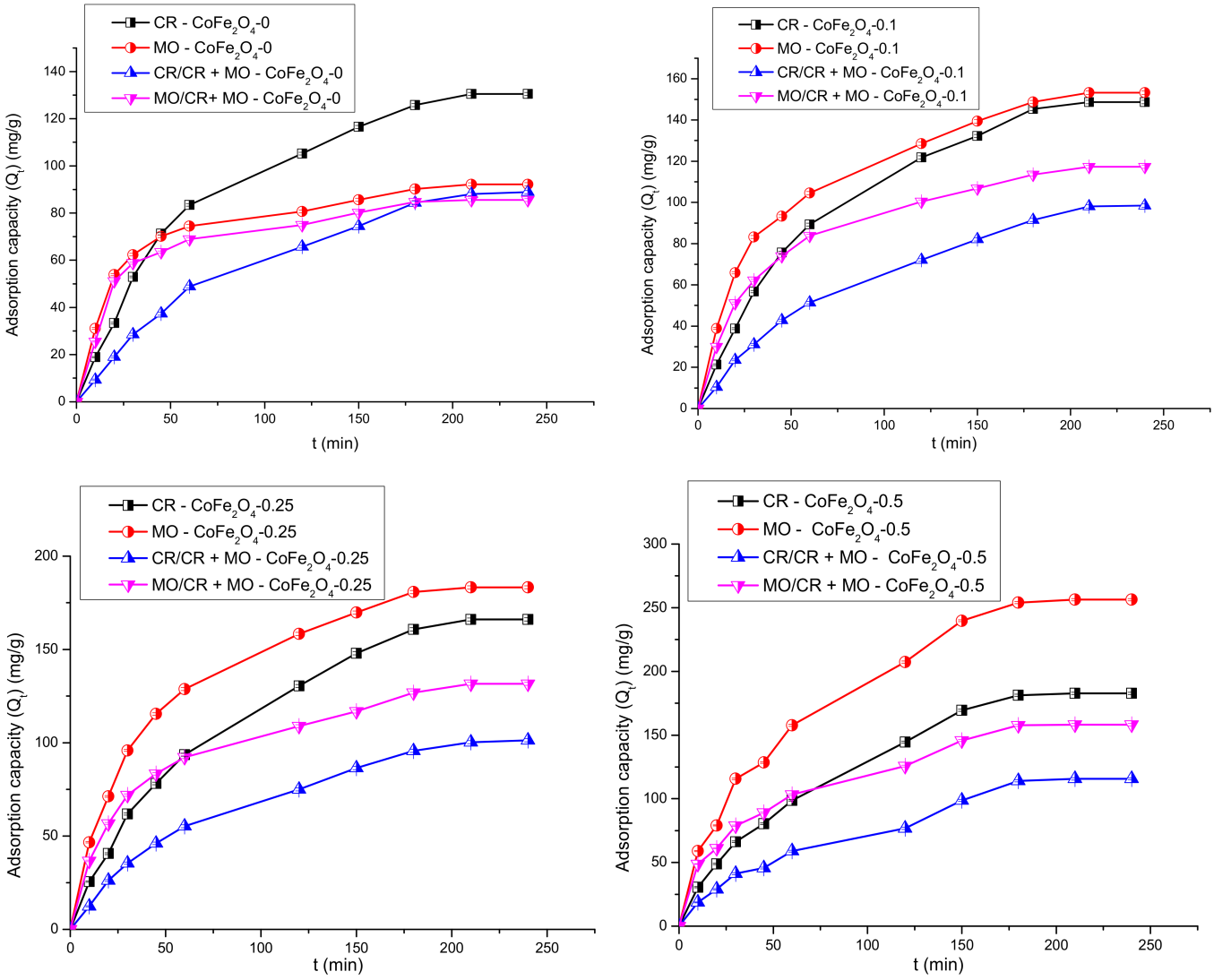

Figure 12. Effect of contact time on the adsorption capacity of $CoFe_2O_4-0$, $CoFe_2O_4-0.1$, $CoFe_2O_4-0.25$, and $CoFe_2O_4-0.5$ from single and binary solutions.

Table 2. The kinetic models used to characterize the CR/MO adsorption onto $CoFe_2O_4$ particles [54].

Kinetic Model	Nonlinear Form of the Kinetic Equation		Defining the Parameters of Mathematical Equations
Pseudo-first-order	$Q_t = Q_e(1 - e^{-k_1 t})$	(4)	k_1—the pseudo-first-order rate constant (min^{-1}), Qe—the adsorption capacity at equilibrium ($mg{\cdot}g^{-1}$), Q_t—the amount of CR/MO adsorbed at time t ($mg{\cdot}g^{-1}$),
Pseudo-second-order	$Q_t = \frac{Q_e^2 k_2 t}{1+Q_e k_2 t}$	(5)	k_2—the rate constant of the pseudo-second-order adsorption process ($g{\cdot}mg^{-1}\ min^{-1}$), Qe—the adsorption capacity at equilibrium ($mg{\cdot}g^{-1}$), Q_t—the amount of CR/MO adsorbed at time t ($mg{\cdot}g^{-1}$),
Intraparticle diffusion	$Q_t = k_{id} t^{0.5} + C$	(6)	k_{id}—the intraparticle diffusion rate constant ($mg{\cdot}g^{-1}{\cdot}\ min^{-1}$), C—the boundary-layer thickness ($mg{\cdot}g^{-1}$).

Figures 13–15 show the pseudo-first order (PFO) and pseudo-second order (PSO) kinetic models fitting the adsorption data for CR and MO in single-component and binary solutions. Tables 3 and 4 display the values of the kinetic parameters calculated using the PFO and PSO nonlinear models in single component and binary solutions, respectively. In the case of CR adsorption, the values of the adjusted R^2 (>0.99) are almost similar for the PFO and PSO models. Considering the consistencies between the experimental and

calculated Q_e values, it seems that the PFO model is more applicable for the removal kinetics of the $CoFe_2O_4$ samples toward the dye. In the case of MO adsorption, the values of the adjusted R^2 (>0.99) are slightly higher for the PSO model than for the PFO model, but the calculated Q_e values from the PSO kinetic model do not agree well with the experimental data. For this reason, it can be considered that the PFO kinetic model is more feasible to describe the adsorption process of MO onto the $CoFe_2O_4$ samples.

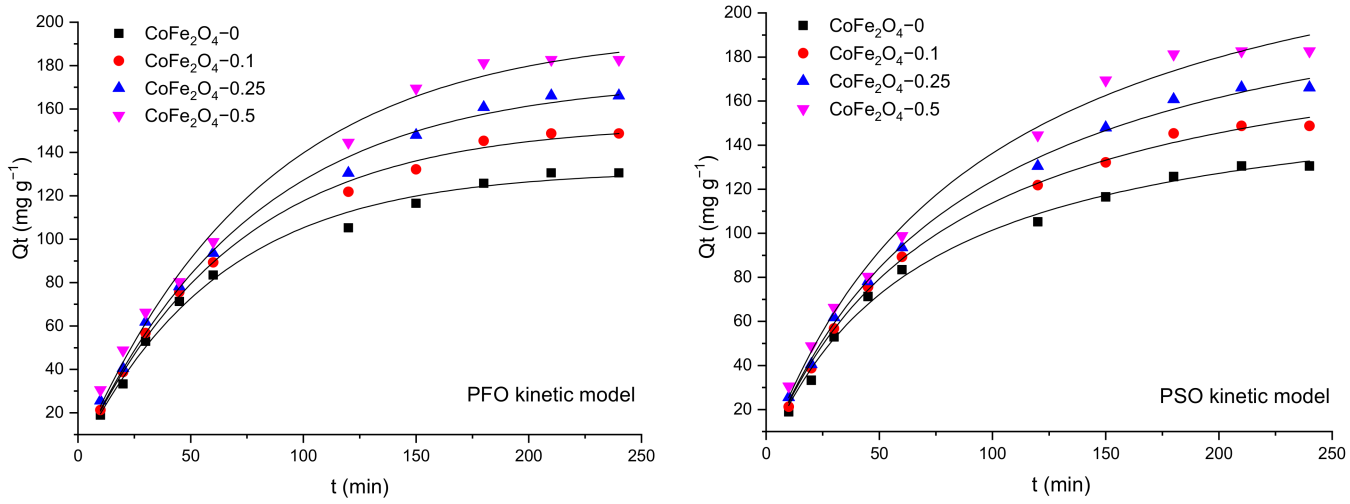

Figure 13. Graphical representation of the PFO and PSO kinetic models for removal of CR by adsorption onto $CoFe_2O_4$ samples from single solutions (nonlinear regression).

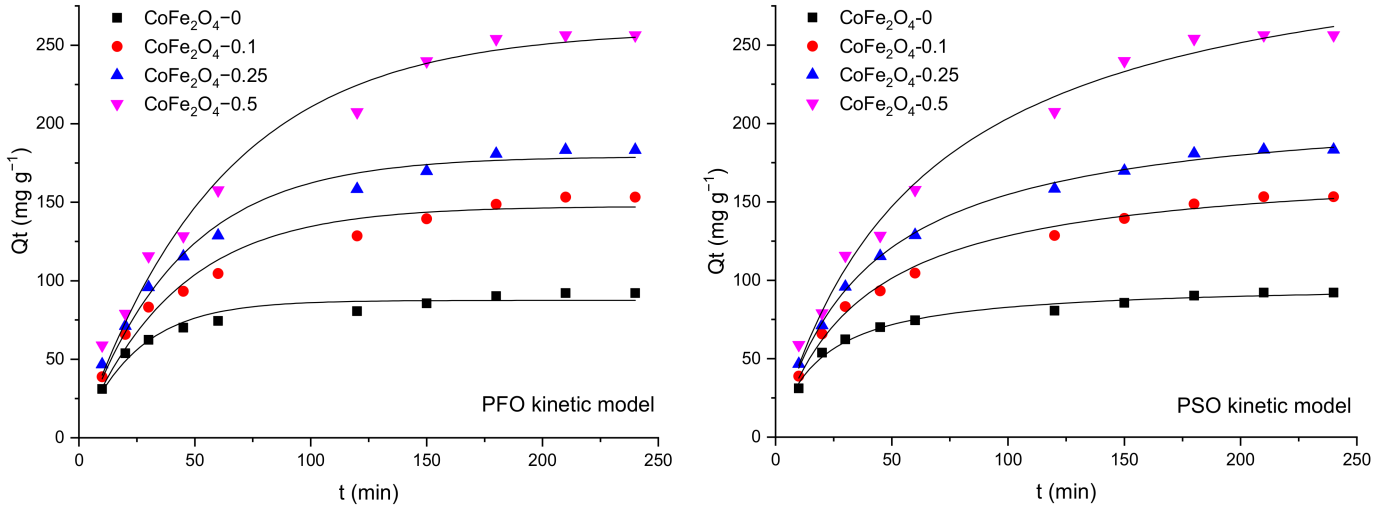

Figure 14. Graphical representation of the PFO and PSO kinetic models for removal of MO by adsorption onto $CoFe_2O_4$ samples from single solutions (nonlinear regression).

According to some studies, external mass transfer occurs at the beginning of the adsorption process, followed by intraparticle diffusion [60]. In the first stage, there is a high concentration gradient between the aqueous and adsorbent surfaces, which causes the solute to migrate faster onto the adsorbent surface. After a period of time, intraparticle diffusion to the adsorbent's internal adsorption sites occurs, which is a sluggish process. This behavior is described by the Weber-Morris model, also known as the intraparticle diffusion model (Equation (6)). According to this model, if a straight line passing through the origin is generated from the plot of Equation (6), it can be inferred that the adsorption mechanism involves intraparticle diffusion of the species. The slope of the linear curve is the rate constant of the intraparticle diffusion process [61]. However, in the current

investigation the plot is not linear and the trend line does not pass through the origin, indicating that intraparticle diffusion is not the only rate-limiting step in dye adsorption on $CoFe_2O_4$ samples. A piecewise linear regression was applied to the experimental data using a Microsoft Excel worksheet developed by Malash and El-Khaiary [62]. The results are presented in Figures 15 and 16 and Table 5. As seen in Figures 16 and 17, the adsorption process can be described based on three stages represented by three straight lines. The first one, characterized by a steep slope, indicates rapid adsorption of the dye at the external surface of the adsorbent. The second stage, in which the slope gradually becomes less slanting, is mainly associated with the diffusion of dye molecules through the internal pores of the adsorbent. The third line is almost horizontal in the last stage, indicating that the equilibrium condition has been reached. This pattern suggests that adsorption is controlled by both external mass transfer and intraparticle diffusion.

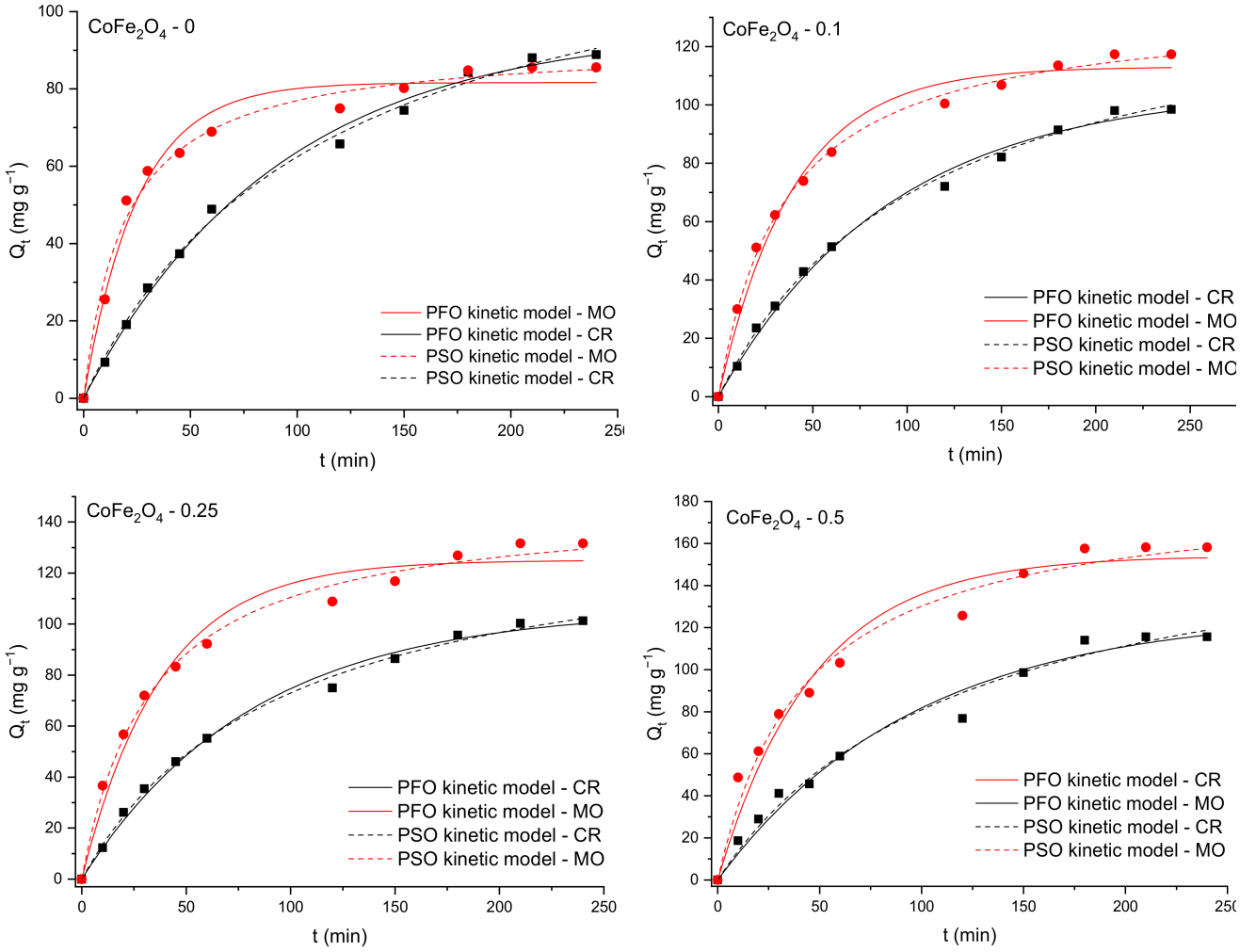

Figure 15. Graphical representation of the PFO and PSO kinetic models for removal of CR and MO by adsorption onto $CoFe_2O_4$ samples from binary solutions (nonlinear regression).

Table 3. The kinetic parameters for dyes adsorption onto $CoFe_2O_4$ samples from single component solutions (nonlinear regression).

Sample	$CoFe_2O_4$-0	$CoFe_2O_4$-0.1	$CoFe_2O_4$-0.25	$CoFe_2O_4$-0.5
		CR		
Q_e exp ($mg \cdot g^{-1}$)	130.51	148.72	166.10	182.71
Pseudo-first-order model				
k_1 (min^{-1})	0.0160 ± 0.0009	0.0145 ± 0.0006	0.0131 ± 0.0007	0.0124 ± 0.0009
Q_e cal ($mg \cdot g^{-1}$)	131.73 ± 2.65	153.29 ± 2.24	173.94 ± 3.56	195.87 ± 5.54
R^2 adjusted	0.9918	0.9965	0.9945	0.9907
Pseudo-second-order model				
k_2 (10^{-4} $g \cdot mg^{-1} \cdot min^{-1}$)	0.8610 ± 0.0910	0.6419 ± 0.0466	0.4869 ± 0.0413	0.4023 ± 0.0577
Q_e cal ($mg \cdot g^{-1}$)	170.50 ± 4.85	201.73 ± 4.08	232.87 ± 5.71	264.43 ± 11.17
R^2 adjusted	0.9935	0.9973	0.9967	0.9912
		MO		
Q_e exp ($mg \cdot g^{-1}$)	92.19	153.29	183.29	256.32
Pseudo-first-order model				
k_1 (min^{-1})	0.0409 ± 0.0037	0.0243 ± 0.0023	0.0235 ± 0.0016	0.0166 ± 0.0015
Q_e cal ($mg \cdot g^{-1}$)	87.50 ± 2.00	147.44 ± 4.15	179.20 ± 3.57	259.83 ± 7.89
R^2 adjusted	0.9471	0.9604	0.9816	0.9776
Pseudo-second-order model				
k_2 (10^{-3} $g \cdot mg^{-1} \cdot min^{-1}$)	0.5522 ± 0.0522	0.1560 ± 0.0146	0.1201 ± 0.0062	0.4885 ± 0.0067
Q_e cal ($mg \cdot g^{-1}$)	98.10 ± 1.71	175.32 ± 3.72	214.72 ± 2.59	329.58 ± 11.88
R^2 adjusted	0.9834	0.9900	0.9970	0.9869

Table 4. The kinetic parameters for dyes adsorption onto $CoFe_2O_4$ samples from binary solutions (nonlinear regression).

Sample	$CoFe_2O_4$-0	$CoFe_2O_4$-0.1	$CoFe_2O_4$-0.25	$CoFe_2O_4$-0.5
		CR		
Q_e exp ($mg \cdot g^{-1}$)	88.87	98.46	101.32	115.64
Pseudo-first-order model				
k_1 (min^{-1})	0.0109 ± 0.0007	0.0108 ± 0.0074	0.0122 ± 0.0087	0.0103 ± 0.0015
Q_e cal ($mg \cdot g^{-1}$)	95.76 ± 2.56	105.66 ± 2.99	105.85 ± 3.56	127.23 ± 8.06
R^2 adjusted	0.9954	0.9948	0.9933	0.9769
Pseudo-second-order model				
k_2 (10^{-4} $g \cdot mg^{-1} \cdot min^{-1}$)	0.6613 ± 0.0740	0.6098 ± 0.0116	0.7253 ± 0.0710	0.4636 ± 0.0084
Q_e cal ($mg \cdot g^{-1}$)	133.25 ± 4.62	146.60 ± 0.8644	143.24 ± 4.15	178.58 ± 102
R^2 adjusted	0.9966	0.9985	0.9968	0.9982
		MO		
Q_e exp ($mg \cdot g^{-1}$)	85.55	117.34	131.65	158.22
Pseudo-first-order model				
k_1 (min^{-1})	0.0396 ± 0.0037	0.0252 ± 0.0019	0.0261 ± 0.0025	0.0212 ± 0.0026
Q_e cal ($mg \cdot g^{-1}$)	81.63 ± 1.94	113.02 ± 2.44	125.02 ± 3.45	154.17 ± 5.77
R^2 adjusted	0.9744	0.9848	0.9742	0.9617
Pseudo-second-order model				
k_2 (10^{-3} $g \cdot mg^{-1} \cdot min^{-1}$)	0.5590 ± 0.0690	0.2130 ± 0.0119	0.2034 ± 0.0019	0.1256 ± 0.0208
Q_e cal ($mg \cdot g^{-1}$)	91.94 ± 2.13	133.91 ± 1.68	147.33 ± 3.07	185.88 ± 7.32
R^2 adjusted	0.9871	0.9977	0.9933	0.9814

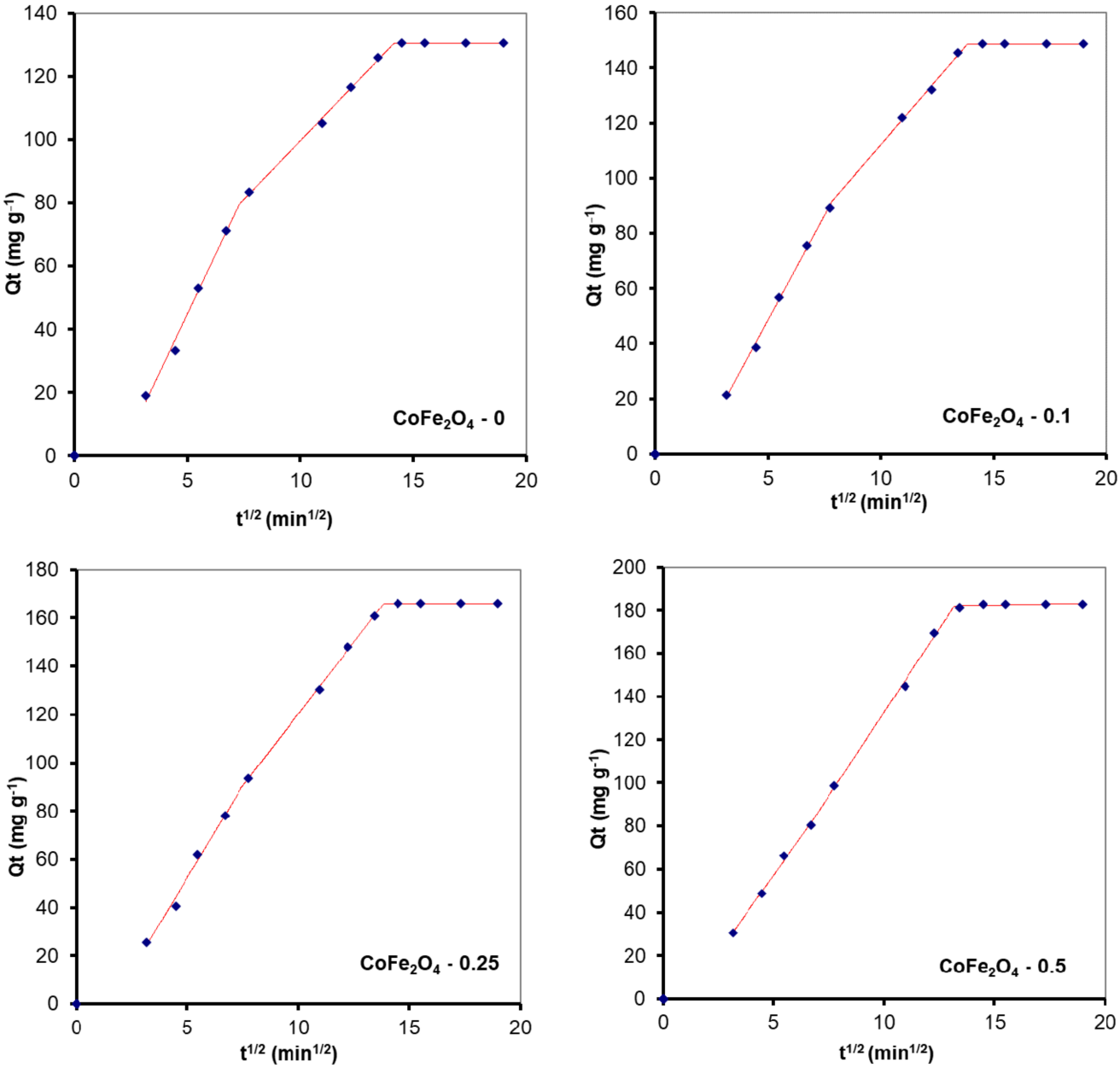

Figure 16. Kinetic modelling of the experimental data obtained from the sorption process of CR onto $CoFe_2O_4$ samples using the intraparticle diffusion model.

3.5.2. The Effect of pH on the Adsorption Performance

The effectiveness and selectivity of a wastewater remediation process by adsorption are influenced by the pH value. It can influence the surface electric charge of the adsorbent and adsorbate and consequently, the nature of the interactions involved in the removal mechanism. The tests regarding the effect of pH on the removal performance of the studied magnetic materials were conducted in the pH range 2–11 and the results are displayed in Figure 18.

Table 5. Kinetic parameters obtained from the fitting of the experimental data with the intraparticle diffusion model.

Sample	Breakpoint ($min^{1/2}$)	k_{id} ($mg \cdot g^{-1} \cdot min^{-1/2}$)	C ($mg \cdot g^{-1}$)	R^2
RC Adsorption				
$CoFe_2O_4$–0	7.3	15.09	−30.67	0.9890
	14.2	7.44	25.15	0.9968
$CoFe_2O_4$–0.1	7.8	15.15	−27.20	0.9978
	13.8	9.50	17.11	0.9906
$CoFe_2O_4$–0.25	7.4	15.32	−24.41	0.9875
	13.8	11.92	0.87	0.9991
$CoFe_2O_4$_0.5	6.7	−14.52	14.34	0.9949
	13.2	−2.18	15.48	0.9948
MO Adsorption				
$CoFe_2O_4$–0	5.72	13.68	−10.70	0.9669
	14.49	2.79	51.64	0.9866
$CoFe_2O_4$–0.1	5.26	20.59	−26.21	0.9999
	13.94	8.16	39.08	0.9985
$CoFe_2O_4$–0.25	6.92	19.78	−15.73	0.9942
	13.70	9.15	57.92	0.9999
$CoFe_2O_4$_0.5	7.74	21.28	−9.68	0.9547
	13.31	17.94	16.13	0.9856

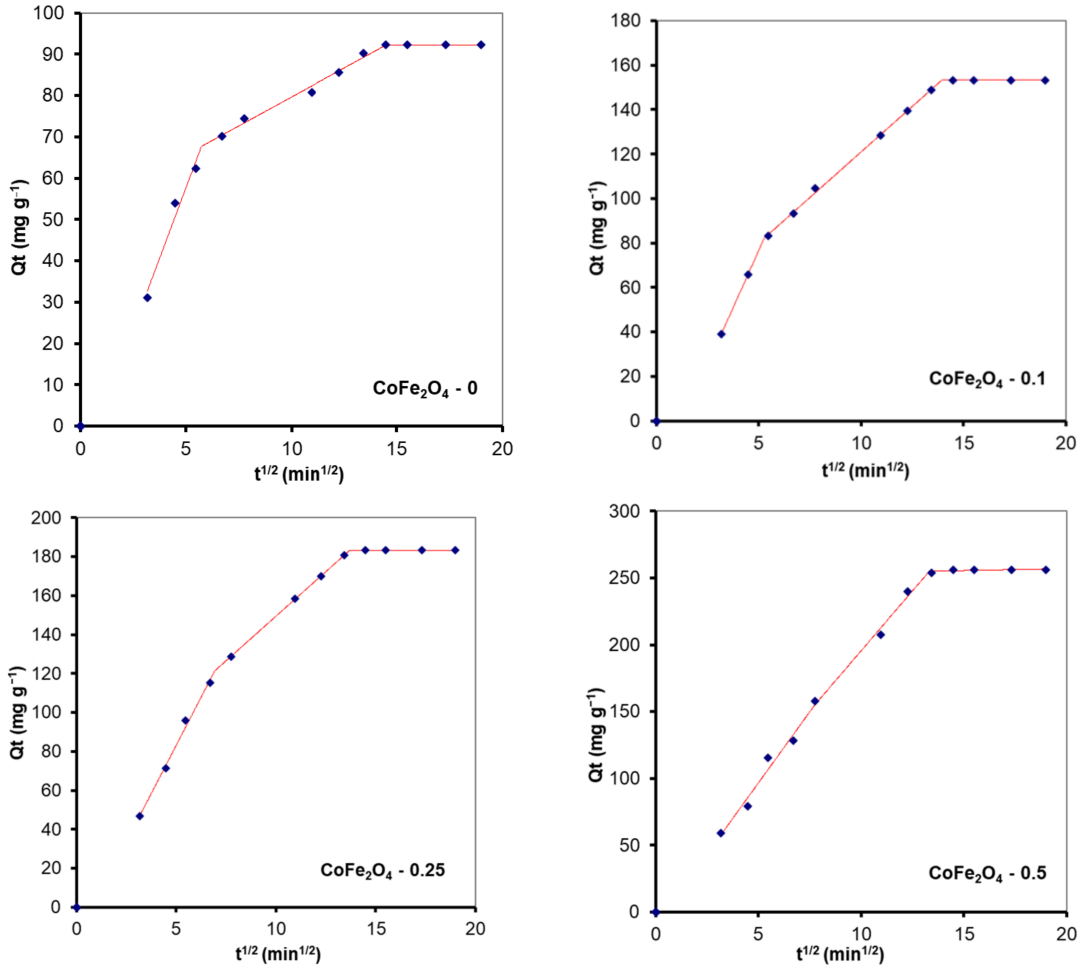

Figure 17. Kinetic modelling of the experimental data obtained from the sorption process of MO onto $CoFe_2O_4$ samples using the intraparticle diffusion model.

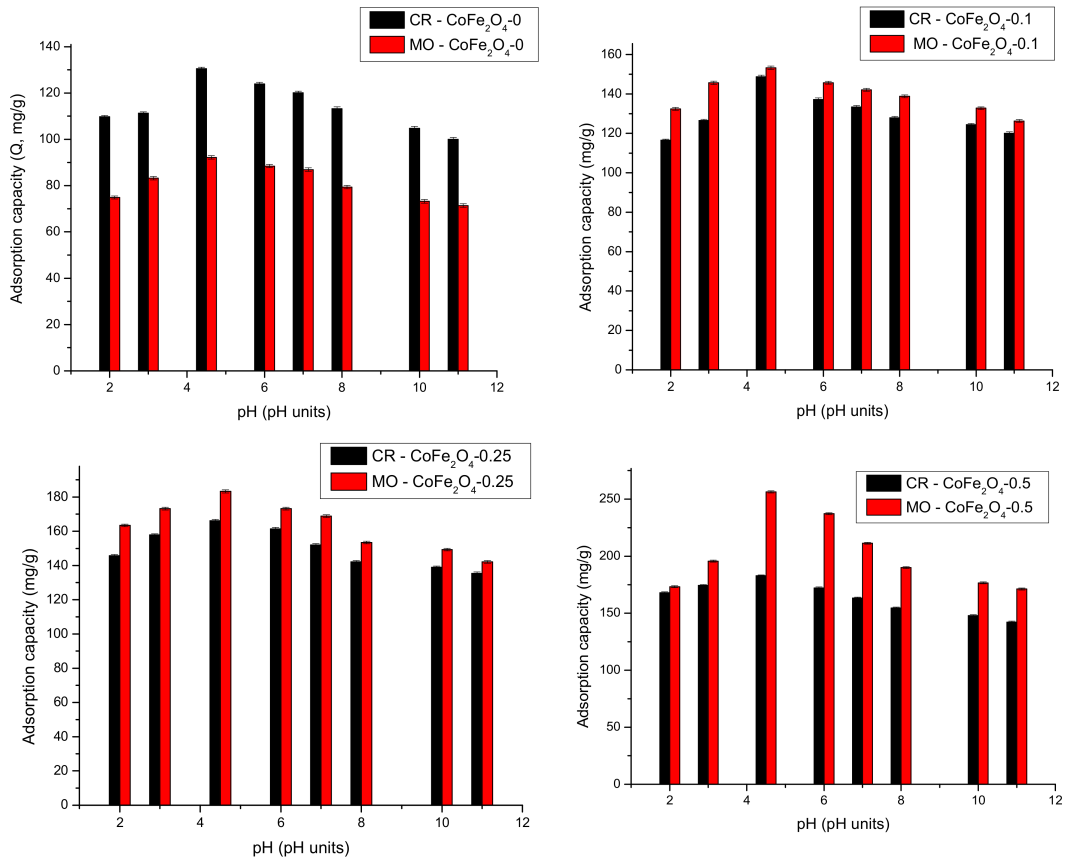

Figure 18. Effect of pH on adsorption capacity of $CoFe_2O_4$ samples for CR/MO from single solutions.

It can be observed that the adsorption capacity of all cobalt ferrite samples increases with the increasing of the solution pH up to 4.5. After this pH value, the adsorption capacity decreases with the increasing of the solution's pH up to 11. This can be explained by the fact that at a lower pH, the positively-charged surface of the $CoFe_2O_4$ samples interacts electrostatically with the negative sulfonate groups of CR/MO. The highest adsorption capacity of the $CoFe_2O_4$ samples was experimentally established to be at a pH of approximately 4.5. At a higher pH, the concentration of OH^- ions continues to increase, competing with the dye molecules for the adsorption sites. Repulsive forces between the dyes and the adsorbent are stronger in basic conditions, hence the adsorption capacity decreases with the increasing of pH values. The results are relatively close to the findings reported by Zwane et al. [13] and Simonescu et al. [54]. The same behavior was found for dye removal from binary solutions. Therefore, the pH value of 4.5 was considered optimal and was used in subsequent experiments.

3.5.3. The Adsorption Isotherms

Adsorption isotherms provide information about the interactions established between the adsorbent and adsorbate during the adsorption process, the mechanism of adsorption, and the efficiency of the adsorbent in terms of its potential to be applied at laboratory, pilot, and industrial scale. Adsorption isotherms describe the relationship between the concentration of the solute retained on the adsorbent surface and its concentration in solution, under well-defined experimental conditions (at optimal contact time and pH, a certain temperature). These values are most often determined experimentally.

Regardless of whether they are inorganic or organic pollutants, the adsorption process can be characterized using the Langmuir and Freundlich isotherms. The nonlinear forms of equations that describe these isotherms are presented in Table 6.

Table 6. The Langmuir and Freundlich nonlinear isotherms.

Isotherm Model	Nonlinear Form of the Isotherm Equation		Defining the Parameters of Mathematical Equations
Langmuir	$Q_e = \frac{Q_{max} K_L C_e}{1+K_L C_e}$	(7)	C_e = equilibrium concentration of the solute in the solution (mg·L^{-1}), K_L = the equilibrium constant of the Langmuir model related to the adsorption energy (L·mg^{-1}), Q_e = the adsorption capacity at equilibrium (mg·g^{-1}), Q_{max} = the maximum adsorption capacity (mg·g^{-1}).
Freundlich	$Q_e = K_F \times C_e^{\frac{1}{n}}$	(8)	K_f and 1/n = Freundlich adsorption isotherm parameters (adsorption capacity (mg·g^{-1}) and intensity), C_e = the equilibrium concentration of the solute in the solution (mg·L^{-1}).

In accordance with the Langmuir isotherm model, it can be stated that the adsorbed molecules form a monolayer on the surface of the adsorbent that is homogeneous (all the adsorption centers are identical) [63]. The Freundlich isotherm is used to characterize a multilayer adsorption process on a heterogeneous surface [63].

In our study, the nonlinear forms of the isotherm equations were applied to characterize the dye adsorption process onto $CoFe_2O_4$ from single solutions. The curve fit of Langmuir and Freundlich isotherms for the two dyes in single and multicomponent solutions are shown in Figures 19 and 20, while the parameters of both isotherms are listed in Table 7. Based on the values of the adjusted R^2, it is obvious that the experimental data for the adsorption of the two dyes onto the $CoFe_2O_4$ samples is appropriately described by the Langmuir model, which implies that the adsorption process of CR and MO takes place on the homogeneous surface of the synthesized cobalt ferrite as a monolayer and each dye molecule does not interact with the neighboring one.

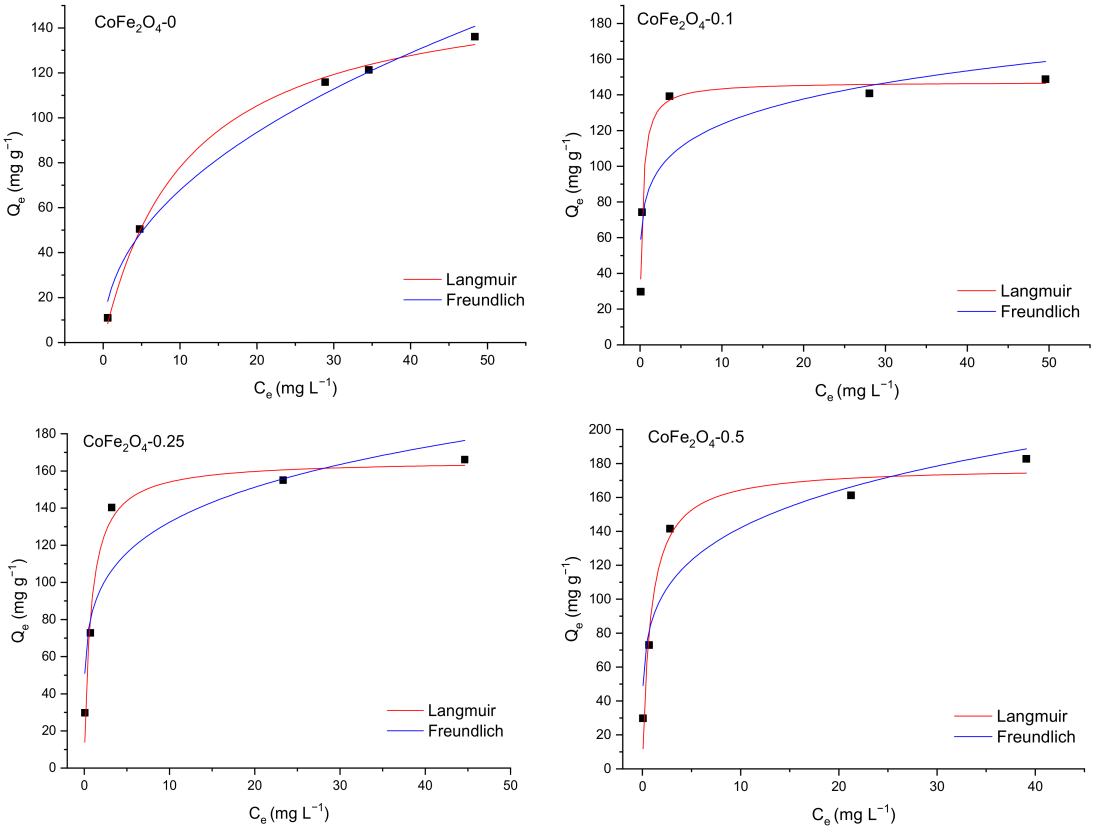

Figure 19. Langmuir and Freundlich fitting curves for CR adsorption onto $CoFe_2O_4$ samples.

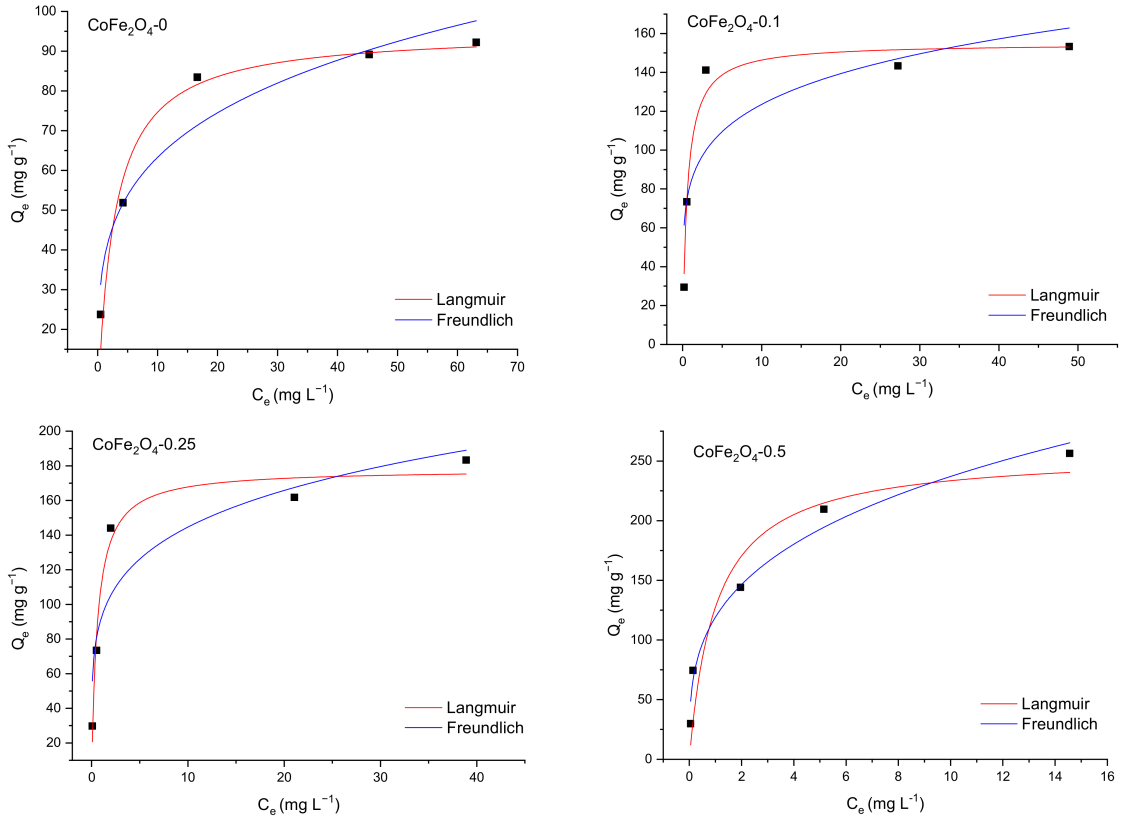

Figure 20. Langmuir and Freundlich fitting curves for MO adsorption onto $CoFe_2O_4$ samples.

Table 7. Langmuir and Freundlich parameters for dye adsorption onto $CoFe_2O_4$ samples from single component solutions.

Dye	**CR**			
Sample	**$CoFe_2O_4$-0**	**$CoFe_2O_4$-0.1**	**$CoFe_2O_4$-0.25**	**$CoFe_2O_4$-0.5**
Langmuir Parameters				
Q_{max} ($mg \cdot g^{-1}$)	162.1564 ± 5.6842	147.2104 ± 3.7878	165.8074 ± 8.4989	178.0762 ± 10.3876
K_L ($L \cdot mg^{-1}$)	0.0927 ± 0.0118	3.7115 ± 0.5291	1.3116 ± 0.3681	1.1944 ± 0.3614
$R^2_{adjusted}$	0.9966	0.9866	0.9616	0.9546
Freundlich Parameters				
K_F ($mg \cdot g^{-1}$)	23.3615 ± 3.7796	86.1721 ± 15.1046	85.0676 ± 14.1775	88.0141 ± 13.3722
1/n	0.4629 ± 0.0454	0.1563 ± 0.0550	0.1920 ± 0.0538	0.2079 ± 0.0502
R^2 adjusted	0.9876	0.7372	0.8310	0.8741
Dye	**MO**			
Sample	**$CoFe_2O_4$-0**	**$CoFe_2O_4$-0.1**	**$CoFe_2O_4$-0.25**	**$CoFe_2O_4$-0.5**
Langmuir Parameters				
Q_{max} ($mg \cdot g^{-1}$)	94.9929 ± 5.1054	154.8871 ± 6.4913	178.0100 ± 8.5675	257.2528 ± 37.9185
K_L ($L \cdot mg^{-1}$)	0.3666 ± 0.1108	1.7089 ± 0.3616	1.6430 ± 0.4021	0.9819 ± 0.6989
R^2 adjusted	0.9533	0.9702	0.9674	0.8802
Freundlich Parameters				
K_F ($mg \cdot g^{-1}$)	36.8004 ± 6.1289	82.7225 ± 17.6008	91.8601 ± 15.7835	119.1167 ± 9.1690
1/n	0.2354 ± 0.0472	0.1740 ± 0.0678	0.1970 ± 0.0570	0.2988 ± 0.0351
R^2 adjusted	0.9107	0.6786	0.8150	0.9718

The maximum value of the adsorption capacity determined from the Langmuir isotherm varies from 162.15 to 178.07 mg g^{-1} for CR and from 94.99 to 257.25 mg g^{-1} for

MO with the increase of the molar ratio $CoFe_2O_4$:DOSS from 1:0 to 1:0.5. The increase of the adsorption capacity is proportional with the increase of the molar ratio $CoFe_2O_4$:DOSS.

For binary solutions, the competitive adsorption capacity of dyes can be evaluated using the modified Langmuir isotherm model. This model is mathematically described by Equation (9) [64].

$$Q_{e,dye1} = \frac{Q_{max,dye1} K_{L,dye1} C_{e,dye1}}{1 + K_{L,dye1} C_{e,dye1} + K_{L,dye2} C_{e,dye2}} \quad (9)$$

Equation (9) is transformed into Equation (10) by linearization:

$$\frac{1}{Q_{e,dye1}} = \frac{1}{Q_{max,dye1}} + \frac{1}{Q_{max,dye1} K_{L,dye1}} \left[\frac{1}{C_{e,dye1}} + \frac{K_{L,dye2} C_{e,dye2}}{C_{e,dye1}} \right] \quad (10)$$

For the second dye from binary solutions, Equation (10) turns into Equation (11):

$$\frac{1}{Q_{e,dye2}} = \frac{1}{Q_{max,dye2}} + \frac{1}{Q_{max,dye2} K_{L,dye2}} \left[\frac{1}{C_{e,dye2}} + \frac{K_{L,dye1} C_{e,dye1}}{C_{e,dye2}} \right] \quad (11)$$

where $C_{e,dye1}$, $C_{e,dye2}$, $Q_{e,dye1}$, and $Q_{e,dye2}$ are the equilibrium concentration and the equilibrium adsorption capacity of dye 1 and dye 2 in the binary systems, $K_{L,dye1}$ and $K_{L,dye2}$ are Langmuir constants characteristics for the dye adsorption from single solutions, $Q_{max,dye1}$ and $Q_{max,dye2}$ are maximum adsorption capacities of dye 1 and dye 2 onto $CoFe_2O_4$ from the binary solution [54,64].

From the linear plot $\frac{1}{Q_{e,dye1}}$ versus $\left[\frac{1}{C_{e,dye1}} + \frac{K_{L,dye2} C_{e,dye2}}{C_{e,dye1}} \right]$ it can be calculated $Q_{max,dye1}$ in binary systems. For the second dye, $Q_{max,dye2}$ can be obtained by the same method using Equation (11).

The ratio $\frac{Q_{max,binary}}{Q_{max,single}}$ provides information regarding the dynamics of dye adsorption in binary systems [65]. When this ratio is suprauntiary, the two adsorbates have a synergistic effect, with the mixture's effect stronger than the individual adsorbate's effect. When the ratio is smaller than one, the two adsorbates have an antagonistic effect, with a weaker effect of the mixture than that of each of the individual adsorbates. When $\frac{Q_{max,binary}}{Q_{max,single}} = 1$, the mixture has no effect on the adsorption of each of the dyes in the mixture [65]. $Q_{max,CR}$ and $Q_{max,MO}$ values, and the ratio $\frac{Q_{max,binary}}{Q_{max,single}}$ for each $CoFe_2O_4$ sample, calculated using the above-described algorithm, are shown in Table 8.

Table 8. Maximum adsorption capacity calculated using Langmuir and modified Langmuir isotherm models for single component and binary solutions.

Adsorbent	Dye	Parameters	Single Component Solution ($mg \cdot g^{-1}$)	Binary Solution ($mg \cdot g^{-1}$)	$\frac{Q_{max,binary}}{Q_{max,single}}$
$CoFe_2O_4$-0	CR	$Q_{max,CR}$	163.89	118.06	0.72
	MO	$Q_{max,MO}$	95.36	120.91	1.26
$CoFe_2O_4$-0.1	CR	$Q_{max,CR}$	149.99	111.23	0.74
	MO	$Q_{max,MO}$	161.09	170.94	1.06
$CoFe_2O_4$-0.25	CR	$Q_{max,CR}$	170.40	214.59	1.25
	MO	$Q_{max,MO}$	187.98	135.31	0.71
$CoFe_2O_4$-0.5	CR	$Q_{max,CR}$	187.10	147.05	0.78
	MO	$Q_{max,MO}$	262.03	116.27	0.44

In the case of CR adsorption, the ratio $\frac{Q_{max,binary}}{Q_{max,single}}$ is smaller than 1 for all adsorbents, excepting $CoFe_2O_4$-0.25, suggesting that the presence of MO inhibits CR adsorption and the mixture has a weaker effect than the individual adsorbates in the mixture. The size of the dye molecules and the texture of the adsorbent both play a role in this phenomenon. Because CR molecules are substantially larger (2.3 nm) than MO molecules (1.2 nm) [66],

it is very likely that the presence of MO molecules in the binary solution will limit their adsorption onto $CoFe_2O_4$ with a porous structure (pore widths between 2.5 and 4.5 nm). In the case of MO adsorption from binary solutions, for the adsorbents with the average pore size $\geq$ 3.5 nm ($CoFe_2O_4$-0 and $CoFe_2O_4$-0.1) the ratio $\frac{Q_{max,binary}}{Q_{max,single}}$ is supraunitary, suggesting a synergistic behavior of the two adsorbates, while for the other two adsorbents, $CoFe_2O_4$-0.25 and $CoFe_2O_4$-0.5, for which the average pore size is smaller than 3.5 nm, the two adsorbates have an antagonistic behavior.

The adsorption capacity of the $CoFe_2O_4$ samples for the removal of CR and MO was compared (Table 9) with those of other similar adsorbents reported in the literature. It is obvious that our samples show superior performance in terms of adsorption of the two dyes, compared to other similar materials.

Table 9. Adsorption capacities of different adsorbents with spinel structure from the literature for the removal of CR and MO.

Dye	Adsorbent	Adsorption Capacity ($mg \cdot g^{-1}$)	Reference
CR	Mo-doped $CoFe_2O_4$	135.14	[67]
	$CoFe_2O_4$	185.4	[68]
	$MnFe_2O_4$	92.4	[40]
	$NiFe_2O_4$	97.1	[40]
	Fe_3O_4	68.5	[40]
	$ZnFe_2O_4$ nanospheres	16.1	[69]
	$Co_{0.3}Ni_{0.7}Fe_2O_4$	131.75	[70]
	$FeFe_2O_4$	97.42	[71]
	$CoFe_2O_4$-0	162.15	This study
	$CoFe_2O_4$-0.1	147.21	This study
	$CoFe_2O_4$-0.25	165.80	This study
	$CoFe_2O_4$-0.5	178.07	This study
MO	$CoFe_2O_4$–FGS nanocomposites	71.54	[72]
	$CuFe_2O_4$@CeO_2 nanofibers	100.0	[73]
	Co_3O_4 nanoparticles	46.08	[74]
	$CoFe_2O_4$	94.33	[75]
	$ZnFe_2O_4$	49.43	[75]
	$Co_{0.5}Zn_{0.5}Fe_2O_4$	67.1	[75]
	$CoFe_2O_4$-0	94.99	This study
	$CoFe_2O_4$-0.1	154.88	This study
	$CoFe_2O_4$-0.25	178.01	This study
	$CoFe_2O_4$-0.5	257.25	This study

Based on the above results, the adsorption behavior of CR or MO by $CoFe_2O_4$ can be mainly assigned to the following: (i) large specific surface area of $CoFe_2O_4$ samples that enhances the mass-transfer process; (ii) the electrostatic interactions between the positively-charged surface of the $CoFe_2O_4$ samples and the negative sulfonate groups of CR/MO; (iii) the H-bonds established between the OH groups of $CoFe_2O_4$ and NH_2/SO^{3-}/azo (-N=N-) groups of CR/MO. The differences between the adsorption capacities of the $CoFe_2O_4$ samples for these two dyes can be explained based on their molecular size [66].

3.5.4. Desorption Study

The regeneration capacity and the possibility to be applied in multiple adsorption-desorption systems are relevant adsorbent properties especially for industrial applications. Ethanol has been tested as a desorbing agent due to its high dipole moments [76]. Six adsorption-desorption cycles in ethanol were applied to determine the reusability of the prepared adsorbents. The results of the adsorption-desorption tests are provided in Figure 21A,B. Desorption efficiency has been determined as well and the results are presented in Figure 22A,B.

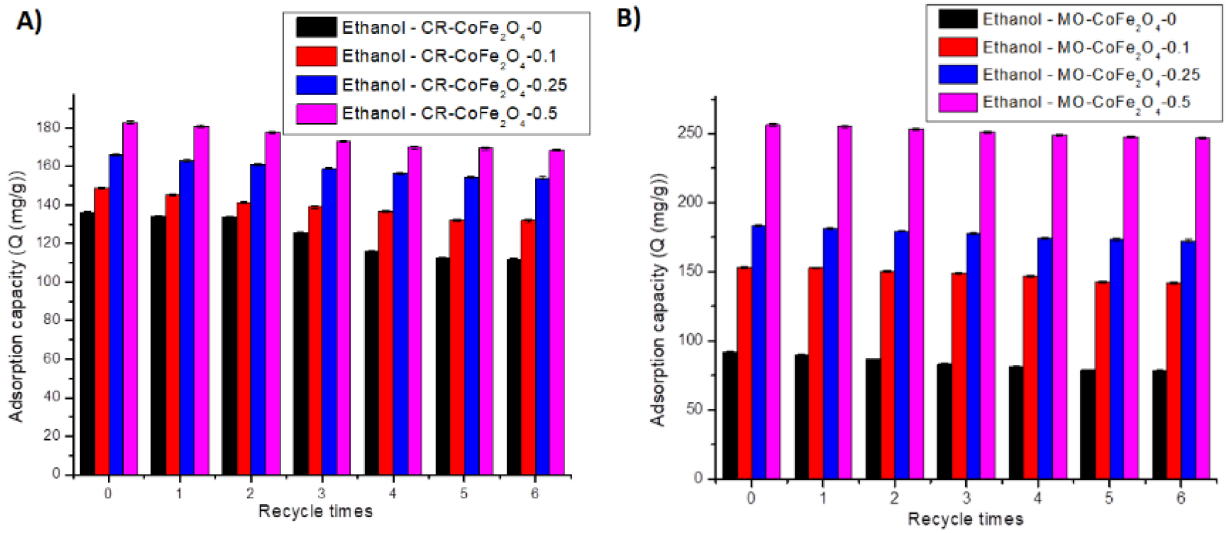

Figure 21. Reusability of $CoFe_2O_4$ samples for CR (**A**) and MO (**B**).

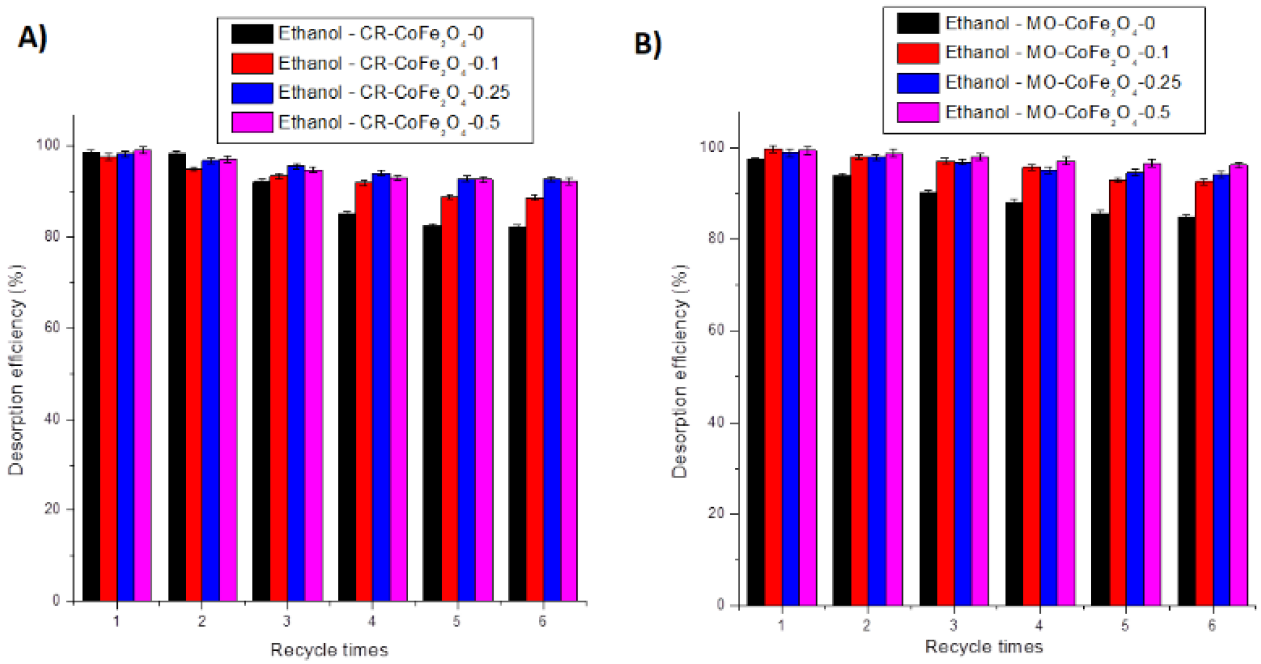

Figure 22. Desorption efficiency of $CoFe_2O_4$ samples for CR (**A**) and MO (**B**).

By analyzing the results presented in Figures 21 and 22, it can be concluded that after six adsorption-desorption tests the maximum decrease of the adsorption capacity was 24.17 $mg \cdot g^{-1}$ for CR and 13.96 $mg \cdot g^{-1}$ for MO, respectively, for the $CoFe_2O_4$-0 sample. The minimum decrease of the adsorption capacity was noticed for the $CoFe_2O_4$-0.5 sample. The desorption efficiency of ethanol varied between 82.24 and 99.01% for CR and between 84.86 and 99.42% for MO, respectively. After six adsorption-desorption consecutive tests, the $CoFe_2O_4$ samples lost 15–18% of the desorption efficiency. This result demonstrates the possibility of using the $CoFe_2O_4$ samples for repetitive adsorption-desorption cycles.

4. Conclusions

In this study, the influence of sodium bis-2-ethyl-hexyl-sulfosuccinate (DOSS) surfactant on the properties of cobalt ferrite nanoparticles (size, shape, texture, and magnetic properties) and also on their ability to remove anionic dyes (Congo Red and Methyl Orange) from synthetic single and binary aqueous solutions was investigated. The obtained

cobalt ferrite nanoparticles have high saturation magnetization (Ms) values ranging from 11.7 to 33.5 emu/g, indicating that they can be isolated quickly and efficiently from solution after adsorption using an external magnetic field. This represents a big advantage because it overcomes the limits of standard separation procedures such as sedimentation and filtration. The effect of different parameters such as contact time and solution pH on the adsorption process was systematically investigated. The results showed that a pH value of 4.5 is the most favorable for CR/MO adsorption. An increase in the adsorption capacity of the $CoFe_2O_4$ samples with the increasing of the quantity of surfactant used in synthesis was observed. The adsorption process was satisfactorily described using the pseudo-first-order kinetic model and the Langmuir isotherm model. The results of the intraparticle diffusion model indicated that the adsorption process is controlled by external mass transfer and intraparticle diffusion.

The maximum adsorption capacity values are higher for MO than for CR in single solutions. In binary solutions it was observed that the presence of MO inhibits CR adsorption, excepting the sample $CoFe_2O_4$-0.25, this behavior being attributed to the size of the dye molecules and the texture of the adsorbent. In the case of MO adsorption from binary solutions, for the adsorbents with the average pore size $\geq$ 3.5 nm ($CoFe_2O_4$-0 and $CoFe_2O_4$-0.1) the two dyes have a synergistic behavior, while for the other two adsorbents with an average pore size smaller than 3.5 nm ($CoFe_2O_4$-0.25 and $CoFe_2O_4$-0.5), the two dyes have an antagonistic behavior. Ethanol was favorably used as a desorbing agent. A small decrease of the adsorption capacity of the $CoFe_2O_4$ samples was observed after six adsorption-desorption cycles. The $CoFe_2O_4$ samples studied in this research can be considered promising materials for removing CR and MO dyes from aqueous solutions in a cost-effective and efficient manner.

Author Contributions: Conceptualization, C.M.S. and A.T.; methodology, C.M.S., A.T. and D.C.C.; software, C.M.S. and D.C.C.; validation, C.M.S., D.C.C. and A.T.; formal analysis, C.M.S. and A.T.; investigation, C.M.S., D.C.C., A.T., N.S., B.B. and A.K.; resources, C.M.S. and A.T.; data curation, C.M.S., D.C.C. and A.T.; writing—original draft preparation, C.M.S., D.C.C., B.B., A.K. and A.T.; writing—review and editing, C.M.S. and D.C.C.; visualization, C.M.S. and A.T.; supervision, D.C.C. All authors have read and agreed to the published version of the manuscript.

Funding: This paper is financed by University Politehnica of Bucharest, being part of the online "Engineer in Europe" project, registered at ME number 140/GP/19.04.2021, by using the special situations funds that cannot be classified as financing the higher state education institutions.

Conflicts of Interest: The authors declare no conflict of interest.

References

1. Raval, N.P.; Shah, P.U.; Shah, N.K. Adsorptive amputation of hazardous azo dye Congo red from wastewater: A critical review. *Environ. Sci. Pollut. Res.* **2016**, *23*, 14810–14853. [CrossRef] [PubMed]
2. Yagub, M.T.; Sen, T.K.; Ang, H.M. Equilibrium, kinetics, and thermodynamics of methylene blue adsorption by pine tree leaves. *Water Air Soil Pollut.* **2012**, *223*, 5267–5282. [CrossRef]
3. Alam, M.S.; Khanom, R.; Rahman, M.A. Removal of Congo Red Dye from Industrial Wastewater by Untreated Sawdust. *Am. J. Environ. Prot.* **2015**, *4*, 207–213. [CrossRef]
4. Hanafi, M.F.; Sapawe, N. A review on the water problem associate with organic pollutants derived from phenol, methyl orange, and remazol brilliant blue dyes. *Mater. Today Proc.* **2020**, *31*, A141–A150. [CrossRef]
5. Garvasis, J.; Prasad, A.R.; Shamsheera, K.O.; Jaseela, P.K.; Joseph, A. Efficient removal of Congo red from aqueous solutions using phytogenic aluminum sulfate nano coagulant. *Mater. Chem. Phys.* **2020**, *251*, 123040. [CrossRef]
6. Habiba, U.; Siddique, T.A.; Joo, T.C.; Salleh, A.; Ang, B.C.; Afifi, A.M. Synthesis of chitosan/polyvinyl alcohol/zeolite composite for removal of methyl orange, Congo red and chromium(VI) by flocculation/adsorption. *Carbohydr. Polym.* **2017**, *157*, 1568–1576. [CrossRef] [PubMed]
7. Zaghloul, A.; Benhiti, R.; Ichou, A.A.; Carja, G.; Soudani, A.; Zerbet, M.; Sinan, F.; Chiban, M. Characterization and application of MgAl layered double hydroxide for methyl orange removal from aqueous solution. *Mater. Today Proc.* **2021**, *37*, 3793–3797. [CrossRef]
8. Zhang, W.; Liang, Y.; Wang, J.; Zhang, Y.; Gao, Z.; Yang, Y.; Yang, K. Ultrasound-assisted adsorption of Congo red from aqueous solution using Mg-Al-CO_3 layered double hydroxide. *Appl. Clay Sci.* **2019**, *174*, 100–109. [CrossRef]

9. Abukhadra, M.R.; Adlii, A.; Bakry, B.M. Green fabrication of bentonite/chitosan@cobalt oxide composite (BE/CH@Co) of enhanced adsorption and advanced oxidation removal of Congo red dye and Cr(VI) from water. *Int. J. Biol. Macromol.* **2019**, *126*, 402–413. [CrossRef]
10. Sathishkumara, K.; AlSalhi, M.S.; Sanganyado, E.; Devanesan, S.; Arulprakash, A.; Rajasekar, A. Sequential electrochemical oxidation and bio-treatment of the azo dye congo red and textile effluent. *J. Photochem. Photobiol. B Biol.* **2019**, *200*, 111655. [CrossRef]
11. Masalvad, S.K.S.; Sakare, P.K. Application of photo Fenton process for treatment of textile Congo-red dye solution. *Mater. Today Proc.* **2021**, *46*, 5291–5297. [CrossRef]
12. Yao, K.; Liu, Y.; Yang, H.; Yuan, J.; Shan, S. Polyaniline-modified 3D-spongy SnS composites for the enhanced visible light photocatalytic degradation of methyl orange. *Colloids Surf. A Physicochem. Eng. Asp.* **2020**, *603*, 125240. [CrossRef]
13. Zwane, S.; Masheane, M.L.; Kuvarega, A.T.; Vilakati, G.D.; Mamba, B.B.; Nyoni, H.; Mhlanga, S.D.; Dlamini, D.S. Polyethersulfone/*Chromolaena odorata* (PES/CO) adsorptive membranes for removal of Congo red from water. *J. Water Process Eng.* **2019**, *30*, 100498. [CrossRef]
14. Li, T.; Zhang, Z.; Liu, L.; Gao, M.; Han, Z. A stable metal-organic framework nanofibrous membrane as photocatalyst for simultaneous removal of methyl orange and formaldehyde from aqueous solution. *Colloids Surf. A Physicochem. Eng. Asp.* **2021**, *617*, 126359. [CrossRef]
15. Edokpayi, J.N.; Makete, E. Removal of Congo red dye from aqueous media using Litchi seeds powder: Equilibrium, kinetics and thermodynamics. *Phys. Chem. Earth* **2021**, *123*, 103007. [CrossRef]
16. Khaniabadi, Y.O.; Heydari, R.; Nourmoradi, H.; Basiri, H.; Basiri, H. Low-cost sorbent for the removal of aniline and methyl orange from liquid-phase: Aloe Vera leaves wastes. *J. Taiwan Inst. Chem. Eng.* **2016**, *68*, 90–98. [CrossRef]
17. Goswami, M.; Chaturvedi, P.; Sonwani, R.K.; Gupta, A.D.; Singhania, R.R.; Giri, B.S.; Rai, B.N.; Singh, H.; Yadav, S.; Singh, R.S. Application of *Arjuna* (*Terminalia arjuna*) seed biochar in hybrid treatment system for the bioremediation of Congo red dye. *Bioresour. Technol.* **2020**, *307*, 123203. [CrossRef]
18. Sonwani, R.K.; Swain, G.; Giri, B.S.; Singh, R.S.; Rai, B.N. Biodegradation of Congo red dye in a moving bed biofilm reactor: Performance evaluation and kinetic modeling. *Bioresour. Technol.* **2020**, *302*, 122811. [CrossRef] [PubMed]
19. Mahmoud, M.E.; Abdou, A.E.H.; Shehata, A.K.; Header, H.M.A.; Hamed, E.A. Sustainable super fast adsorptive removal of Congo red dye from water by a novel technique based on microwave-enforced sorption process. *J. Ind. Eng. Chem.* **2018**, *57*, 28–36. [CrossRef]
20. Chan, Y.Y.; Pang, Y.L.; Lim, S.; Chong, C.W. Sonocatalytic degradation of Congo red by using green synthesized silver doped zinc oxide nanoparticles. *Mater. Today Proc.* **2021**, *46*, 1948–1953. [CrossRef]
21. Ma, M.; Ying, H.; Cao, F.; Wang, Q.; Ai, N. Adsorption of congo red on mesoporous activated carbon prepared by CO_2 physical activation. *Chin. J. Chem. Eng.* **2020**, *28*, 1069–1076. [CrossRef]
22. Yönten, V.; Sanyürek, N.K.; Kivanç, M.R. A thermodynamic and kinetic approach to adsorption of methyl orange from aqueous solution using a low cost activated carbon prepared from *Vitis vinifera* L. *Surf. Interfaces* **2020**, *20*, 100529. [CrossRef]
23. Yu, K.L.; Lee, X.J.; Ong, H.C.; Chen, W.-H.; Chang, J.-S.; Lin, C.-S.; Show, P.L.; Ling, T.C. Adsorptive removal of cationic methylene blue and anionic Congo red dyes using wet-torrefied microalgal biochar: Equilibrium, kinetic and mechanism modeling. *Environ. Pollut.* **2021**, *272*, 115986. [CrossRef]
24. Wang, Z.; Li, Y.; Xie, X.; Wang, Z. Bifunctional $MnFe_2O_4$/chitosan modified biochar composite for enhanced methyl orange removal based on adsorption and photo-Fenton process. *Colloids Surf. A Physicochem. Eng. Asp.* **2021**, *613*, 126104. [CrossRef]
25. Arab, C.; El Kurdi, R.; Patra, D. Efficient removal of Congo red using curcumin conjugated zinc oxide nanoparticles as new adsorbent complex. *Chemosphere* **2021**, *276*, 130158. [CrossRef] [PubMed]
26. Ahmed, S.; Ur Rehman, H.; Ali, Z.; Qadeer, A.; Haseeb, A.; Ajmal, Z. Solvent assisted synthesis of hierarchical magnesium oxide flowers for adsorption of phosphate and methyl orange: Kinetic, isotherm, thermodynamic and removal mechanism. *Surf. Interfaces* **2021**, *23*, 100953. [CrossRef]
27. Zhang, P.; Wang, T.; Qian, G.; Wu, D.; Frost, R.L. Removal of methyl orange from aqueous solutions through adsorption by calcium aluminate hydrates. *J. Colloid Interface Sci.* **2014**, *426*, 44–47. [CrossRef]
28. Adebayo, M.A.; Adebomi, J.I.; Abe, T.O.; Areo, F.I. Removal of aqueous Congo red and malachite green using ackee apple seed–bentonite composite. *Colloids Interface Sci. Commun.* **2020**, *38*, 100311. [CrossRef]
29. Zayed, A.M.; Abdel Waheda, M.S.M.; Mohamed, E.A.; Sillanpää, M. Insights on the role of organic matters of some Egyptian clays in methyl orange adsorption: Isotherm and kinetic studies. *Appl. Clay Sci.* **2018**, *166*, 49–60. [CrossRef]
30. Borth, K.W.; Galdino, C.W.; de Carvalho Teixeira, V.; Anaissi, F.J. Iron oxide nanoparticles obtained from steel waste recycling as a green alternative for Congo red dye fast adsorption. *Appl. Surf. Sci.* **2021**, *546*, 149126. [CrossRef]
31. Srilakshmi, C.; Saraf, R. Ag-doped hydroxyapatite as efficient adsorbent for removal of Congo red dye from aqueous solution: Synthesis, kinetic and equilibrium adsorption isotherm analysis. *Micropor. Mesopor. Mater.* **2016**, *219*, 134–144. [CrossRef]
32. Karthikeyan, P.; Elanchezhiyan, S.S.D.; Banu, H.A.T.; Farzana, M.H.; Park, C.M. Hydrothermal synthesis of hydroxyapatite-reduced graphene oxide (1D-2D) hybrids with enhanced selective adsorption properties for methyl orange and hexavalent chromium from aqueous solutions. *Chemosphere* **2021**, *276*, 130200. [CrossRef]
33. Raza, S.; Wen, H.; Peng, Y.; Zhang, J.; Li, X.; Liu, C. Fabrication of SiO_2 modified biobased hydrolyzed hollow polymer particles and their applications as a removal of methyl orange dye and bisphenol-A. *Eur. Polym. J.* **2021**, *144*, 110199. [CrossRef]

34. Sulaiman, N.S.; Zaini, M.A.A.; Arsad, A. Evaluation of dyes removal by beta-cyclodextrin adsorbent. *Mater. Today Proc.* **2021**, *39*, 907–910. [CrossRef]
35. Yang, Z.; Liu, L.; Liu, S.; Su, G.; Liu, X.; Tang, A.; Xue, J.; Zeng, M. Synthesis of dithiocarbamate-modified crosslinked poly(β−cyclodextrin-co-triethylenetetramine) micro-spheres for simultaneous and highly efficient removal of Cu^{2+} and methyl orange/thymol blue from wastewater. *React. Funct. Polym.* **2021**, *159*, 104809. [CrossRef]
36. Ghosh, S.; Sarkar, A.; Chatterjee, S.; Nayek, H.P. Elucidation of selective adsorption study of Congo red using new Cadmium(II) metal-organic frameworks: Adsorption kinetics, isotherm and thermodynamics. *J. Solid State Chem.* **2021**, *296*, 121929. [CrossRef]
37. Tor, A.; Cengeloglu, Y. Removal of congo red from aqueous solution by adsorption onto acid activated red mud. *J. Hazard. Mater.* **2006**, *B138*, 409–415. [CrossRef]
38. Kumari, D.; Mazumder, P.; Kumar, M.; Deka, J.P.; Shim, J. Simultaneous removal of Cong red and Cr(VI) in aqueous solution by using Mn powder extracted from battery waste solution. *Groundw. Sustain. Dev.* **2018**, *7*, 459–464. [CrossRef]
39. Mishra, S.; Sahoo, S.S.; Debnath, A.K.; Muthe, K.P.; Das, N.; Parhi, P. Cobalt ferrite nanoparticles prepared by microwave hydrothermal synthesis and adsorption efficiency for organic dyes: Isotherms, thermodynamics and kinetic studies. *Adv. Powder Technol.* **2020**, *31*, 4552–4562. [CrossRef]
40. Wang, L.; Li, J.; Wang, Y.; Zhao, L.; Jiang, O. Adsorption capability for Congo red on nanocrystalline MFe_2O_4 (M = Mn, Fe Co, Ni) spinel ferrites. *Chem. Eng. J.* **2012**, *181*, 72–79. [CrossRef]
41. Adel, M.; Ahmed, M.A.; Mohamed, A.A. Effective removal of indigo carmine dye from wastewaters by adsorption onto mesoporous magnesium ferrite nanoparticles. *Environ. Nanotechnol. Monit. Manag.* **2021**, *16*, 100550. [CrossRef]
42. An, S.; Liu, X.; Yang, L.; Zhang, L. Enhancement removal of crystal violet dye using magnetic calcium ferrite nanoparticle: Study insingle- and binary-solute systems. *Chem. Eng. Res. Des.* **2015**, *94*, 726–735. [CrossRef]
43. Mahmoodi, N.M.; Abdi, J.; Bastani, D. Direct dyes removal using modified magnetic ferrite nanoparticle. *J. Environ. Health Sci. Eng.* **2014**, *12*, 96. [CrossRef]
44. Humelnicu, A.-C.; Cojocaru, C.; Pascariu Dorneanu, P.; Samoila, P.; Harabagiu, V. Novel chitosan-functionalized samarium-doped cobalt ferrite for adsorptive removal of anionic dye from aqueous solutions. *Compets Rendus Chim.* **2017**, *20*, 1026–1036. [CrossRef]
45. Moghaddam, A.Z.; Ghiamati, E.; Pourashuri, A.; Allahresani, A. Modified nickel ferrite nanocomposite/functionalized chitosan as a novel adsorbent for the removal of acidic dyes. *Int. J. Biol. Macromol.* **2018**, *120*, 1714–1725. [CrossRef]
46. Jayalakshmi, R.; Jeyanthi, J. Dynamic modelling of Alginate—Cobalt ferrite nanocomposite for removal of binary dyes from textile effluent. *J. Environ. Chem. Eng.* **2021**, *9*, 104924. [CrossRef]
47. Culita, D.C.; Simonescu, C.M.; Dragne, M.; Stanica, N.; Munteanu, C.; Preda, S.; Oprea, O. Effect of surfactant concentration on textural, morphological and magnetic properties of $CoFe_2O_4$ nanoparticles and evaluation of their adsorptive capacity for Pb(II) ions. *Ceram. Int.* **2015**, *41*, 13553–13560. [CrossRef]
48. Amirthavalli, C.; Thomas, J.M.; Nagaraj, K.; Prince, A.A.M. Facile room temperature CTAB-assisted synthesis of mesoporous nano-cobalt ferrites for enhanced magnetic behavior. *Mater. Res. Bull.* **2018**, *100*, 289–294. [CrossRef]
49. De Medeiros, F.; Madigou, V.; Lopes-Moriyama, A.L.; Pereira de Souza, C.; Leroux, C. Synthesis of $CoFe_2O_4$ nanocubes. *Nano-Struct. Nano-Objects* **2020**, *21*, 100422. [CrossRef]
50. Rana, S.; Philip, J.; Raj, B. Micelle based synthesis of cobalt ferrite nanoparticles and its characterization using Fourier Transform Infrared Transmission Spectrometry and Thermogravimetry. *Mater. Chem. Phys.* **2010**, *124*, 264–269. [CrossRef]
51. Maaz, K.; Mumtaz, A.; Hasanain, S.K.; Ceylan, A. Synthesis and magnetic properties of cobalt ferrite ($CoFe_2O_4$) nanoparticles prepared by wet chemical route. *J. Magn. Magn. Mater.* **2007**, *308*, 289–295. [CrossRef]
52. Singh, M.; Dosanjh, H.S.; Singh, H. Surface modified spinel cobalt ferrite nanoparticles for cationic dye removal: Kinetics and thermodynamics studies. *J. Water Process Eng.* **2016**, *11*, 152–161. [CrossRef]
53. Tătăruş, A.; Simonescu, C.M.; Nechifor, G.; Scutariu, R.; Iancu, V.I.; Chiriac, L.F. Development of a new high-performance liquid chromatography method with diode array detector (HPLC-DAD) for the detection of Congo Red and Methyl Orange dyes from synthetic water solutions. *UPB Sci. Bull. Ser. B* **2021**, *83*, 4, in press.
54. Simonescu, C.M.; Tătăruş, A.; Culiţă, D.C.; Stănică, N.; Ionescu, I.A.; Butoi, B.; Banici, A.-M. Comparative Study of $CoFe_2O_4$ Nanoparticles and $CoFe_2O_4$-Chitosan Composite for Congo Red and Methyl Orange Removal by Adsorption. *Nanomaterials* **2021**, *11*, 711. [CrossRef]
55. Das, S.; Bououdina, M.; Manoharan, C. The influence of cationic surfactant CTAB on optical, dielectric and magnetic properties of cobalt ferrite nanoparticles. *Ceram. Int.* **2020**, *46*, 11705–11716. [CrossRef]
56. Mahdikhah, V.; Ataie, A.; Babaei, A.; Sheibani, S.; Ow-Yang, C.W.; Khabbaz Abkenar, S. Control of structural and magnetic characteristics of cobalt ferrite by post-calcination mechanical milling. *J. Phys. Chem. Solids* **2019**, *134*, 286–294. [CrossRef]
57. Shafi, V.P.M.K.; Gedanken, A.; Prozorov, R.; Balogh, J. Sonochemical Preparation and Size-Dependent Properties of Nanostructured $CoFe_2O_4$ Particles. *Chem. Mater.* **1998**, *10*, 3445–3450. [CrossRef]
58. Emadi, H.; Kharat, A.N. Synthesis and characterization of ultrafine and mesoporous structure of cobalt ferrite. *J. Ind. Eng. Chem.* **2015**, *21*, 951–956. [CrossRef]
59. Baraka, A. Investigation of temperature effect on surface-interaction and diffusion of aqueous-solution/porous-solid adsorption systems using diffusion—binding model. *J. Environ. Chem. Eng.* **2015**, *3*, 129–139. [CrossRef]
60. Alkan, M.; Demirbas, O.; Dogan, M. Adsorption kinetics and thermodynamics of an anionic dye onto sepiolite. *Microporous Mesoporous Mater.* **2007**, *101*, 388–396. [CrossRef]

61. Kumar, P.A.; Ray, M.; Chakraborty, S. Adsorption behaviour of trivalent chromium on amine-based polymer aniline formaldehyde condensate. *Chem. Eng. J.* **2009**, *149*, 340–347. [CrossRef]
62. Malash, G.F.; El-Khaiary, M.I. Piecewise linear regression: A statistical method for the analysis of experimental adsorption data by the intraparticle-diffusion models. *Chem Eng. J.* **2010**, *163*, 256–263. [CrossRef]
63. Zhang, P.; Lo, I.; O'Connor, D.; Pehkonen, S.; Cheng, H.; Hou, D. High efficiency removal of methylene blue using SDS surface-modified $ZnFe_2O_4$ nanoparticles. *J. Colloid Interface Sci.* **2017**, *508*, 39–48. [CrossRef]
64. Manjunath, S.V.; Kumar, M. Evaluation of single-component and multi-component adsorption of metronidazole, phosphate and nitrate on activated carbon from *Prosopis juliflora*. *Chem. Eng. J.* **2018**, *346*, 525–534. [CrossRef]
65. Mahamadi, C.; Nharingo, T. Competitive adsorption of Pb^{2+}, Cd^{2+} and Zn^{2+} ions onto *Eichhornia crassipes* in binary and ternary systems. *Bioresour. Technol.* **2010**, *101*, 859–864. [CrossRef]
66. Wu, Q.; Liang, H.; Li, M.; Liu, B.; Xu, Z. Hierarchically porous carbon membranes derived from PAN and their selective adsorption of organic dyes. *Chin. J. Polym. Sci.* **2016**, *34*, 23–33. [CrossRef]
67. Amar, I.A.; Asser, J.O.; Mady, A.S. Adsorptive removal of congo red dye from aqueous solutions using Mo-doped $CoFe_2O_4$ magnetic nanoparticles. *Pigment. Resin Technol.* **2021**, *50*, 6, 563–573. [CrossRef]
68. Zhang, L.; Lian, J.; Wang, L.; Jiang, J.; Duan, Z.; Zhao, L. Markedly enhanced coercive field and Congo red adsorption capability of cobalt ferrite induced by the doping of non-magnetic metal ions. *Chem. Eng. J.* **2014**, *241*, 384–392. [CrossRef]
69. Rahimi, R.; Kerdari, H.; Rabbani, M.; Shafiee, M. Synthesis, characterization and adsorbing properties of hollow Zn–Fe_2O_4 nanospheres on removal of Congo red from aqueous solution. *Desalination* **2011**, *280*, 412–418. [CrossRef]
70. Chen, R.; Wang, W.; Zhao, X.; Zhang, Y.; Wu, S.; Li, F. Rapid hydrothermal synthesis of magnetic $Co_xNi_{1-x}Fe_2O_4$ nanoparticles and their application on removal of Congo red. *Chem. Eng. J.* **2014**, *242*, 226–233. [CrossRef]
71. Wang, Y.Q.; Cheng, R.M.; Wen, Z.; Zhao, L. Investigation on the room temperature preparation and application of chain-like iron flower and its ramifications in wastewater purification. *Chem. Eng. J.* **2012**, *203*, 277–284. [CrossRef]
72. Li, N.; Zheng, M.; Chang, X.; Ji, G.; Lu, H.; Xue, L.; Pan, L.; Cao, J. Preparation of magnetic $CoFe_2O_4$-functionalized graphene sheets via a facile hydrothermal method and their adsorption properties. *J. Solid State Chem.* **2011**, *184*, 953–958. [CrossRef]
73. Zou, L.; Wang, Q.; Shen, X.; Wang, Z.; Jing, M.; Luo, Z. Fabrication and dye removal performance of magnetic $CuFe_2O_4$@CeO_2 nanofibers. *Appl. Surf. Sci.* **2015**, *332*, 674–681. [CrossRef]
74. Uddin, M.K.; Baig, U. Synthesis of Co_3O_4 nanoparticles and their performance towards methyl orange dye removal: Characterisation, adsorption and response surface methodology. *J. Clean. Prod.* **2019**, *211*, 1141–1153. [CrossRef]
75. Thomas, B.; Alexander, L.K. Enhanced synergetic effect of Cr(VI) ion removal and anionic dye degradation with superparamagnetic cobalt ferrite meso–macroporous nanospheres. *Appl. Nanosci.* **2018**, *8*, 125–135. [CrossRef]
76. Mittal, H.; Al Alili, A.; Morajkar, P.P.; Alhassan, S.M. Graphene oxide crosslinked hydrogel nanocomposites of xanthan gum for the adsorption of crystal violet dye. *J. Mol. Liq.* **2021**, *323*, 115034. [CrossRef]